

# Probing the nucleosynthetic contribution of low-metallicity, low-mass star companions of CEMP stars\*

J. SHEJEELAMMAL<sup>1</sup> AND ARUNA GOSWAMI<sup>1</sup>

<sup>1</sup>Indian Institute of Astrophysics, Koramangala, Bangalore 560034, India

(Received XXX; Revised XXX; Accepted XXX)

Submitted to ApJ

## ABSTRACT

The observed abundance diversities among the CEMP stars can shed light on the formation and evolution of elements in the early Galaxy. In this work, we present results obtained from a detailed abundance analysis of a sample of seven extrinsic carbon stars. The analysis is based on high-resolution spectra obtained with HCT/HESP (R~60,000) and SUBARU/HDS (R~50,000). We present, for the first time, the elemental abundance results for the objects BD-19 132, BD-19 290, HE 1304-2111, HE 1354-2257, and BD+19 3109. Abundances of a few elements are available in literature for HE 1157-0518 and HD 202851, we present an update on the abundances of these elements along with new abundance estimates for several other elements. Our analysis confirms the object HD 202851 to be a CH star. While BD-19 132, HE 1354-2257, and BD+19 3109 are found to be CEMP-s stars, the objects BD-19 290, HE 1157-0518, and HE 1304-2111 are found to belong to CEMP-r/s group. The observed abundance patterns of the three CEMP-r/s stars are well reproduced with the i-process model predictions. While the objects BD+19 3109 and HD 202851 are confirmed binaries, the binary status of the remaining objects are not known. Analysis based on different elemental abundance ratios confirms low-mass former AGB companions for all the objects. Kinematic analysis shows that BD-19 290, HE 1157-0518, HE 1354-2257, and BD+19 3109 belong to the Galactic halo, whereas BD-19 132, HE 1304-2111, and HD 202851 are members of Galactic thin disk.

*Keywords:* stars: Abundances - stars: chemically peculiar - stars: carbon - stars: individual

## 1. INTRODUCTION

Being enriched with carbon (and neutron-capture elements), the atmospheres of the low-mass, metal-poor stars in the Galaxy bear the fingerprints of the chemical evolution history of the Galaxy. They are the window to the early Galaxy, as they preserve in their atmosphere the chemical imprints of the gas clouds from which they were formed. For this reason, metal-poor stars such as CH stars and Carbon-Enhanced Metal-Poor (CEMP) stars, have been extensively studied in the last few decades for the information they provide on the origin and evolution of elements in the early Galaxy. A number of large sky survey programs to identify

the most metal-poor stars were conducted in the past such as HK survey (Beers et al. 1985, 1992, 2007; Beers 1999), Hamburg/ESO Survey (HES; Christlieb et al. 2001a,b; Christlieb 2003; Christlieb et al. 2008), Sloan Digital Sky Survey (SDSS; York et al. 2000), and LAMOST (Large Sky Area Multi-Object Fiber Spectroscopic Telescope) survey (Cui et al. 2012; Deng et al. 2012; Zhao et al. 2012). These surveys have revealed that a significant fraction (~20%) of Very Metal-Poor ([Fe/H]<-2) stars in the Galaxy are CEMP stars (Rossi et al. 1999; Christlieb 2003; Lucatello et al. 2006; Carollo et al. 2012). The fraction of carbon-enhanced stars increases with decreasing metallicity; ~40% for [Fe/H]<-3 and ~75% for [Fe/H]<-4 (Aoki et al. 2013; Lee et al. 2013; Yong et al. 2013; Placco et al. 2014; Frebel & Norris 2015).

CH stars ( $-2 \leq [\text{Fe}/\text{H}] \leq -0.2$ ) are characterized by the strong CH and C<sub>2</sub> molecular bands, C/O>1 and strong features due to the neutron-capture elements

Corresponding author: Aruna Goswami  
aruna@iiap.res.in

\* Based on data collected using HCT/HESP and SUBARU/HDS

(Keenan 1942). CEMP stars are more metal-poor counterparts of CH stars ( $[\text{Fe}/\text{H}] < -1$ ; Lucatello et al. 2005; Abate et al. 2016) which has been traditionally defined as the stars with  $[\text{C}/\text{Fe}] > 1$  (Beers & Christlieb 2005). However, the definition of CEMP stars is being revised and  $[\text{C}/\text{Fe}] \geq 0.70$  (Aoki et al. 2007; Carollo et al. 2012; Lee et al. 2013; Norris et al. 2013b; Skúladóttir et al. 2015) and  $[\text{C}/\text{Fe}] > 0.90$  (Jonsell et al. 2006; Masseron et al. 2010) are also used.

Based on the level of relative enrichment of neutron-capture elements, CEMP stars are classified into different sub-classes; CEMP-s (show enhanced abundances of s-process elements), CEMP-r (show strong enhancement of r-process elements), CEMP-r/s (show simultaneous enhancement of both s- and r-process elements) and CEMP-no (does not show any enhanced abundance of neutron-capture elements). This diverse abundance pattern observed in the CEMP stars points to different formation scenarios. The CEMP-s stars are considered as the metal-poor analog of Ba and CH stars, and the binary mass transfer from an evolved low-mass AGB companion is the most accepted scenario for their abundance peculiarity (Herwig 2005). The long-term radial velocity monitoring studies have shown that most of the CEMP-s stars are binaries (Lucatello et al. 2005; Starkenburg et al. 2014; Jorissen et al. 2016; Hansen et al. 2016b), supporting the pollution from companion AGB. Comparison of observed abundances in the CEMP-s stars with theoretical model predictions also confirms the binary mass-transfer from the AGB companion (Bisterzo et al. 2011; Placco et al. 2013; Hollek et al. 2015).

There exist several proposed scenarios for the abundance pattern in CEMP-r/s stars that show enhancement in both s- and r-process elements that are ascribed to different astrophysical sites. The proposed scenarios for CEMP-r/s stars include; binary system formed out of r-enriched ISM, pollution of binary system from a massive tertiary, pollution from the binary companion exploded as Type 1.5 SNe (Accretion Induced Collapse, AIC) etc. (Jonsell et al. 2006 and references therein). However, none of these proposed scenarios is able to reproduce the observed abundance trend and frequency of CEMP-r/s stars (Abate et al. 2016). Since most of the CEMP-r/s stars are also found to be binaries just like CEMP-s stars, binary mass transfer from the AGB companion is thought to be the reason for their origin as well, however the presence of r-process component posed a challenge (Jonsell et al. 2006; Herwig et al. 2011; Abate et al. 2016). The i-process, intermediate neutron-capture process, with neutron density between s- and r-process can produce both s- and r- process elements at

a single stellar site (Cowan & Rose 1977). Many studies in literature have successfully used model yields of i-process in low-mass low-metallicity AGB stars to account for the observed abundance patterns in CEMP-r/s stars (Hempel et al. 2016, 2019; Goswami et al. 2021; Shejeelammal et al. 2021). Although there are several suggestions for the i-process sites (super-massive AGB stars (Doherty et al. 2015; Jones et al. 2016), low-mass low-metallicity stars (Campbell & Lattanzio 2008; Campbell et al. 2010; Cruz et al. 2013; Cristallo et al. 2016), Rapidly Accreting White Dwarfs (Herwig et al. 2014; Denissenkov et al. 2017) etc.) the exact astrophysical site for the i-process is not yet confirmed (Frebel 2018; Koch et al. 2019).

The origins of CEMP-no and CEMP-r stars are also not clearly understood. CEMP-r stars are rare among all the CEMP sub-classes. Analysis of Hansen et al. (2011) and Hansen et al. (2015a) have shown that the abundance peculiarity of CEMP-r stars is not resulted from a binary mass transfer, instead due to the enrichment of their birth cloud from other external sources. Various suggested progenitors of the CEMP-r stars that polluted the ISM with r-elements are core-collapse SNe (Qian 2000; Argast et al. 2004; Arcones & Thielemann 2013), fallback SNe (Fryer et al. 2006), neutron star mergers (Tanvir et al. 2013; Rosswog et al. 2014; Drout et al. 2017; Lippuner et al. 2017) or neutron star - black hole mergers (Surman et al. 2008). The observations of more such stars are required to constrain their exact origin. Similar to CEMP-r stars, the observed carbon enhancement in CEMP-no stars is also believed to be from the pre-enriched ISM (Norris et al. 2013a; Cooke & Madau 2014; Frebel & Norris 2015). The suggested progenitors of CEMP-no stars include faint SNe (Umeda & Nomoto 2005; Nomoto et al. 2013; Tominaga et al. 2014), spin-star (Meynet et al. 2010; Chiappini 2013), metal-free massive stars (Heger & Woosley 2010). A recent study by Arentsen et al. (2019a) have shown that the binary mass-transfer from an extremely metal-poor AGB companion could also be a possible progenitor of the CEMP-no stars.

In this study, we have carried out a detailed spectroscopic analysis of seven carbon stars selected from various sources in literature, in order to understand their formation history from a detailed abundance analysis. The structure of this paper is as follows. Section 2. describes the stellar sample, source of the spectra and the data reduction. The derivation of stellar atmospheric parameter, radial velocity estimation and stellar mass determination are discussed in Section 3. The details of abundance determination is described in Section 4 and

a discussion on abundance uncertainties is presented in Section 5. Section 6. provides the details of kinematic analysis. In Section 7, the classification of program stars based on the observed abundances is presented. Section 8 presents a discussion on various elemental abundance ratios and their interpretations. A discussion on the binary status of the program stars and on the individual stars along with the parametric model based analysis are also given in this section. Finally, conclusions are drawn in Section 9.

## 2. STELLAR SAMPLE: SELECTION, OBSERVATION/DATA ACQUISITION AND DATA REDUCTION

Out of the total seven objects analyzed in this study, four objects, BD–19 132, BD–19 290, BD+19 3109, and HD 202851 are selected from the catalog of CH star by Bartkevicius (1996). The other three objects, HE 1157–0518, HE 1304–2111, and HE 1354–2257 are selected from the candidate metal-poor stars identified in Hamburg/ESO survey (HES) (Christlieb 2003) and in the HK survey of Beers et al. (1992). The stars HE 1157–0518 and HE 1354–2257 are also listed in the catalog of carbon stars identified from Hamburg/ESO survey (HES) by Christlieb et al. (2001a). The spectra of the objects BD–19 132, BD–19 290, BD+19 3109, and HD 202851 at a resolution  $(\lambda/\delta\lambda)\sim 60,000$  are obtained using high-resolution Hanle Echelle Spectrograph (HESP) attached to the 2m Himalayan Chandra Telescope (HCT) operated at the Indian Astronomical Observatory, Hanle. For all these four objects, we have taken three frames each with an exposure of 2700 sec and then co-added to improve the quality (S/N ratio) of the resulting spectra. This S/N ratio enhanced spectra are then used for further analysis. The wavelength span of HCT/HESP spectra is 3530 - 9970 Å. The spectra of the objects HE 1157–0518, HE 1304–2111, and HE 1354–2257 at a resolution  $(\lambda/\delta\lambda)\sim 50,000$  were taken from the SUBARU/HDS archive (<http://jvo.nao.ac.jp/portal/v2/>). The High Dispersion Spectrograph (HDS) is an echelle spectrograph of 8.2m SUBARU telescope (Noguchi et al. 2002) at Hawaii, operated by National Astronomical Observatory of Japan (NAOJ). The SUBARU spectra covers 4100 - 6850 Å in wavelength with a wavelength gap between 5440 and 5520 Å due to the separation between the two CCDs used. The data is further reduced using

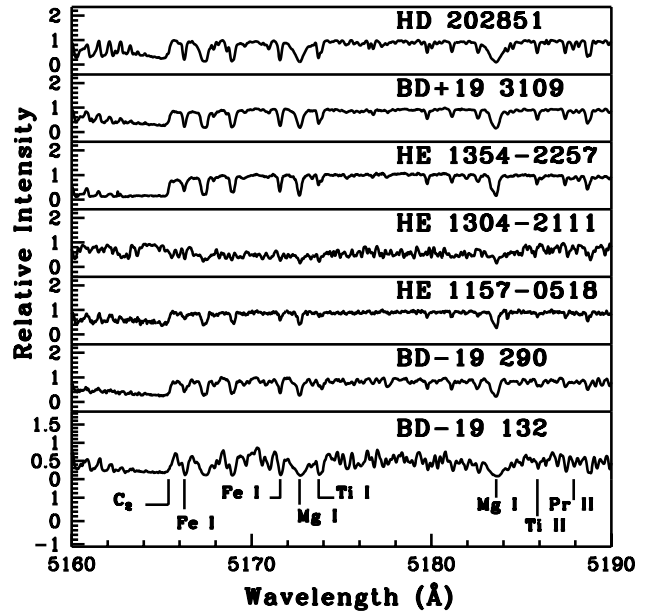


**Figure 1.** Sample spectra of the program stars in the wavelength region 5160 to 5190 Å.

IRAF<sup>1</sup> software. The basic information of the program stars are given in Table 1 and some sample spectra of the program stars are shown in Figure 1.

## 3. STELLAR ATMOSPHERIC PARAMETERS AND RADIAL VELOCITY

The radial velocities of the program stars are calculated from the Doppler equation using the measured wavelength shift of a set of clean spectral lines of several elements. Our radial velocity estimates along with that from Gaia DR2 (Gaia Collaboration et al. 2018) are presented in Table 2. Radial velocity data are not available in literature for the stars HE 1157–0518 and HE 1354–2257. While the objects BD–19 290, HE 1157–0518, HE 1354–2257 and BD+19 3109 are found to be high velocity objects with  $V_r$  in the range  $-181.8$  to  $+289.4$  km s<sup>-1</sup>, BD–19 132, HE 1304–2111, and HD 202851 are low velocity objects with  $V_r$  in the range 2.1 to  $+22.2$  km s<sup>-1</sup>. The objects BD+19 3109 and HD 202851 are confirmed binaries with periods of  $2129\pm 13$  and  $1295\pm 6$  days respectively (Sperauskas et al. 2016). The estimated radial velocities of these two objects differ by  $\sim 5$  km s<sup>-1</sup> from the literature values available in Gaia archive. For the objects BD–19 132, BD–19 290, and HE 1304–2111 our

<sup>1</sup> IRAF (Image Reduction and Analysis Facility) is distributed by the National Optical Astronomical Observatories, which is operated by the Association for Universities for Research in Astronomy, Inc., under contract to the National Science Foundation

**Table 1. Primary information of the program stars.**

Star	RA(2000)	Dec.(2000)	B	V	J	H	K	Exposure (seconds)	Date of obs.	Source of spectrum	4200 Å	S/N 5500 Å	7700 Å
BD-19 132	00 50 24.16	-19 04 40.19	13.25	10.73	8.083	7.354	7.070	2700(3)	07/11/2017	HESP	11.37	30.71	40.93
BD-19 290	01 40 34.11	-18 56 51.52	12.41	11.07	8.710	8.102	7.914	2700(3)	08/11/2017	HESP	6.41	23.59	47.07
HE 1157-0518	12 00 08.06	-05 34 43.12	16.273	15.120	13.418	12.917	12.846	1800	25/05/2003	SUBARU	9.32	25.15	-
HE 1304-2111	13 07 27.26	-21 27 34.24	14.547	13.061	9.651	9.009	8.764	1200	25/05/2003	SUBARU	5.21	21.53	-
HE 1354-2257	13 57 43.30	-23 12 34.55	15.22	14.00	11.809	11.290	11.110	1800	26/05/2003	SUBARU	6.39	35.56	-
BD+19 3109	16 29 26.99	+19 30 34.46	11.88	10.29	8.051	7.40	7.253	2700(3)	23/05/2018	HESP	7.80	48.27	95.90
HD 202851	21 18 43.49	-01 32 03.34	10.89	9.67	7.711	7.174	7.029	2700(3)	07/11/2017	HESP	17.01	31.82	54.57

The number of frames taken are given with exposure time, in parenthesis.

estimates show a difference of  $\sim 13$ ,  $6$ , and  $17$   $\text{km s}^{-1}$  respectively from those listed in Gaia archive. This may be an indication that these stars could possibly be binaries.

The procedure adopted for deriving the atmospheric parameters of the program stars is explained in detail in our previous papers Shejeelammal et al. (2020, 2021). Here we briefly mention a few relevant points. The equivalent width measured from a set of clean Fe I and Fe II lines are used for the derivation of the stellar atmospheric parameters. The lines are selected such that they have equivalent width and excitation potential in the range  $8 - 180$  mÅ and  $0 - 6$  eV respectively. We have used the most recent version of the radiative transfer code MOOG by Sneden (Sneden 1973) employing Local Thermodynamic Equilibrium (LTE) for our analysis. The photometric temperatures of the program stars are calculated using the color-temperature calibration equations of Alonso et al. (1999, 2001) and used as initial guess of effective temperatures for model calculation. With this temperature estimate and a guess of  $\log g$  value typical of giants, the initial model atmospheres are selected from the Kurucz grid of model atmosphere with no convective overshooting (<http://kurucz.harvard.edu/grids.html>). The excitation balance of Fe I lines is employed to fix the final effective temperature. The zero slope between the measured equivalent widths and the abundances of Fe I lines gives the microturbulent velocity. Finally, the ionization balance between the Fe I and Fe II gives the surface gravity. The final model atmosphere is adopted from the initial one through an iterative process until these three conditions are satisfied simultaneously. Once this is achieved,  $[\text{Fe}/\text{H}]$  is estimated from the derived iron abundance. The abundances derived from Fe I and Fe II lines as functions of excitation potentials and equivalent widths are shown in Figure 2. The derived atmospheric parameters along with the available literature values of the program stars are given in Table 2.

We have also estimated the  $\log g$  value using the standard equation  $\log (g/g_{\odot}) = \log (M/M_{\odot}) + 4 \log (T_{\text{eff}}/T_{\text{eff}\odot}) - \log (L/L_{\odot})$

We have adopted the solar values  $\log g_{\odot} = 4.44$ ,  $T_{\text{eff}\odot} = 5770\text{K}$  and  $M_{\text{bol}\odot} = 4.74$  mag. The detailed procedure is given in Shejeelammal et al. (2020). The luminosity,  $\log (L/L_{\odot})$ , is calculated using the V magnitudes taken from SIMBAD astronomical database and the parallaxes ( $\pi$ ) taken from Gaia DR2 (Gaia Collaboration et al. 2018, <https://gea.esac.esa.int/archive/>). The bolometric correction and the interstellar extinction required for the calculation of luminosity are estimated using the calibration equation of Alonso et al. (1999) and Chen et al. (1998) respectively. With this calculated luminosity and spectroscopic temperature estimate, the mass is found from the position of the star on Hertzsprung - Russell (HR) diagram ( $\log T_{\text{eff}}$  v/s  $\log (L/L_{\odot})$ ). The HR diagram is generated using the stellar evolutionary tracks of Girardi et al. (2000). Thus  $\log g$  is calculated with this mass using the above equation. We have used  $z = 0.0004$  tracks for the objects BD-19 290 and HE 1157-0518 and  $z=0.004$  tracks for HD 202851. These HR diagrams are shown in Figure 3. For the objects BD-19 132, HE 1304-2111, HE 1354-2257, and BD+19 3109, we could not determine their masses as the tracks corresponding to their luminosity and temperatures are not available. The mass estimates and  $\log g$  values estimated from the parallax method are given in Table 3. For our analysis, we have used the spectroscopic  $\log g$  values.

#### 4. ABUNDANCE DETERMINATION

The elemental abundances are derived by two methods; from the measured equivalent widths of spectral lines due to several elements and the spectral synthesis calculation. The spectral lines of different elements are identified by comparing the spectrum of Arcturus with the spectra of the program stars. The line parameters, excitation potential and oscillator strength ( $\log gf$ ) values, are taken from Kurucz database of atomic line lists (<https://lweb.cfa.harvard.edu/amp/ampdata/kurucz23/sekur.html>). The abundances from the molecular bands are derived using the spectral synthesis calculation. For the elements showing the hyper-fine splitting (HFS), spectral synthesis calculation is performed in addition to the abundance derived from the equivalent width measurements. In the case of elements with NLTE effects,

**Table 2.** Derived atmospheric parameters of the program stars.

Star	$T_{\text{eff}}$ (K)	$\log g$ cgs	$\zeta$ (km s <sup>-1</sup> )	[Fe I/H]	[Fe II/H]	$V_r$ (km s <sup>-1</sup> )	$V_r$ (km s <sup>-1</sup> )	Reference
	$\pm 100$	$\pm 0.2$	$\pm 0.2$			(This work)	(Gaia)	
BD-19 132	4005	1.13	2.02	-1.86±0.06	-1.86±0.01	+3.94±0.81	+16.97±0.79	1
BD-19 290	4315	0.61	3.10	-2.86±0.07	-2.86±0.13	+106.28±0.90	+111.99±0.73	1
HE 1157-0518	5050	2.52	2.15	-2.42±0.15	-2.42±0.16	+116.02±0.70	-	1
	4900	2.00	-	-2.40	-	-	-	2
HE 1304-2111	4325	1.06	0.63	-2.34±0.10	-2.34±0.07	+2.14±0.34	+19.33±0.59	1
HE 1354-2257	4700	1.13	1.86	-2.11±0.17	-2.11±0.15	+289.46±1.80	-	1
BD+19 3109	4035	0.75	2.05	-2.23±0.09	-2.23±0.02	-181.89±1.38	-187.09±1.55	1
HD 202851	4900	2.20	1.54	-0.85±0.11	-0.85±0.05	+22.22±0.90	+17.38±1.22	1
	4800	2.10	1.50	-0.70	-	-	-	3
	4733	1.60	-	-0.88	-	-	-	4

References: 1. This work, 2. [Aoki et al. \(2007\)](#), 3. [Sperauskas et al. \(2016\)](#), 4. [Arentsen et al. \(2019b\)](#)

**Table 3.** Mass and log g estimated from parallax method

Star name	Parallax (mas)	$M_{\text{bol}}$	$\log(L/L_{\odot})$	Mass( $M_{\odot}$ )	$\log g$ (cgs)	$\log g$ (spectroscopic) (cgs)
BD-19 132	0.3556±0.0560	-2.395±0.345	2.854±0.138	-	-	1.13
BD-19 290	0.1449±0.0417	-3.745±0.334	3.390±0.260	1.00±0.40	0.54±0.07	0.61
HE 1157-0518	0.0778±0.0397	-0.725±1.222	2.186±0.490	1.00±0.60	2.02±0.25	2.52
HE 1304-2111	22.7558±0.040	9.229±0.004	-1.797±0.002	-	-	1.06
HE 1354-2257	0.0150±0.0514	5.638±3.231	4.151±1.292	-	-	1.13
BD+19 3109	0.3764±0.0284	-2.765±0.165	3.000±0.060	-	-	0.75
HD 202851	2.2160±0.0982	0.955±0.999	1.514±0.040	1.05±0.05	2.66±0.02	2.20

appropriate NLTE corrections have been applied to the estimated abundances. The details of the abundance derivation of each element along with the details of HFS and the NLTE corrections used are discussed in the following. The derived elemental abundances of the program stars are presented in Table 4 and 5 and the lines used are given in Table A1 and A2. The abundance ratios are calculated with respect to solar value ([Asplund et al. 2009](#)).

4.1. *Light elements: C, N, O, <sup>12</sup>C/<sup>13</sup>C, Na,  $\alpha$ -, and Fe-peak elements*

The abundance of oxygen is derived from the spectral synthesis calculation of [O I] 6300.304 Å line. This line is insensitive to NLTE effect. The other oxygen forbidden line at 6363.776 Å is not usable for the abundance determination in any of the program stars. The O I triplet lines around 7770 Å was not good in the stars BD-19 132, BD-19 290, BD+19 3109, and HD 202851. In the other three stars this region is absent as the SUBARU spectra is limited up to 6850 Å. We could determine the oxygen abundance only in four stars: BD-19 132, BD-19 290, HE 1354-2257, and

HD 202851, with BD-19 290 showing the highest enhancement of [O/Fe]~1.34. In other three stars [O/Fe] ranges from 0.23 to 0.51.

Once the oxygen abundance is determined, the carbon abundance is derived from the C<sub>2</sub> molecular bands at 5165 and 5635 Å by spectral synthesis calculation. The spectral synthesis fits for these two regions for a few program stars are shown in Figure 4. The C<sub>2</sub> bands at 5165 Å is noisy in the spectra of BD-19 132 and HE 1304-2111; so we could not use this region in these stars. In all other stars, we derived the carbon abundance from both the regions. The abundances derived from these two bands are consistent within 0.3 dex. The average abundance from these two C<sub>2</sub> regions is taken as the final carbon abundance. All the stars except BD-19 132 and HD 202851 show [C/Fe]>1, with BD+19 3109 being the most carbon enhanced with [C/Fe]~2.47.

The nitrogen abundance is derived from the <sup>12</sup>CN lines at 8000 Å region in the program stars that are observed with HESP and from <sup>12</sup>CN band at 4215 Å region in the spectra obtained with SUBARU. We could determine nitrogen abundance in all the stars except HE 1304-2111.

**Table 4.** Elemental abundances in BD–19 132, BD–19 290, HE 1157–0518, and HE 1304–2111

	Z	BD–19 132			BD–19 290			HE 1157–0518			HE 1304–2111			
		solar $\log \epsilon^*$	$\log \epsilon$	[X/H]	[X/Fe]	$\log \epsilon$	[X/H]	[X/Fe]	$\log \epsilon$	[X/H]	[X/Fe]			
C (C <sub>2</sub> band 5165 Å)	6	8.43	-	-	-	7.35(syn)	-1.08	1.78	8.18(syn)	-0.25	2.17	-	-	
C (C <sub>2</sub> band 5635 Å)	6	8.43	7.27(syn)	-1.16	0.70	7.58(syn)	-0.85	2.01	8.45(syn)	0.02	2.44	8.33(syn)	-0.10	2.24
<sup>12</sup> C/ <sup>13</sup> C	-	-	-	-	18	-	-	4	-	-	-	-	-	-
N	7	7.83	7.43(syn)(3)	-0.40	1.46	6.86(syn)(3)	-0.97	1.89	6.93(syn)	-0.90	1.52	-	-	-
O	8	8.69	7.06(syn)(1)	-1.63	0.23	7.17(syn)(1)	-1.52	1.34	-	-	-	-	-	-
Na I	11	6.24	5.47±0.07(2)	-0.77	1.09	4.56±0.13(2)	-1.68	1.18	-	-	-	6.73±0.12(2)	0.49	2.83
Mg I	12	7.60	6.32±0.02(2)	-1.28	0.58	5.35(1)	-2.25	0.61	5.45(1)	-2.15	0.27	5.46(1)	-2.12	0.22
Si I	14	7.51	-	-	-	-	-	-	-	-	-	5.91±0.01(2)	-1.60	0.74
Ca I	20	6.34	5.21±0.11(4)	-1.13	0.73	3.93±0.05(4)	-2.41	0.45	4.07±0.13(4)	-2.27	0.15	4.49±0.16(2)	-1.85	0.49
Sc II	21	3.15	2.09(syn)(1)	-1.06	0.80	1.10±0.07(syn)(2)	-2.05	0.81	1.35(syn)(1)	-1.80	0.62	1.45(syn)(1)	-1.70	0.64
Ti I	22	4.95	3.68±0.14(7)	-1.27	0.59	2.28±0.0(2)	-2.67	0.19	2.36(1)	-2.59	-0.17	3.07±0.14(3)	-1.88	0.46
Ti II	22	4.95	3.42±0.13(7)	-1.53	0.33	2.17±0.03(3)	-2.78	0.08	2.59±0.17(3)	-2.36	0.06	2.54(1)	-2.41	-0.07
V I	23	3.93	1.93(syn)(1)	-2.00	-0.14	2.13(syn)(1)	-1.80	1.06	1.75(syn)(1)	-2.18	0.24	2.99±0.23(syn)(2)	-0.94	1.40
Cr I	24	5.64	-	-	-	-	-	-	3.18±0.11(2)	-2.46	-0.04	4.43±0.11(4)	-1.21	1.13
Cr II	24	5.64	-	-	-	3.80±0.10(2)	-1.84	1.02	-	-	-	-	-	-
Mn I	25	5.43	3.50(syn)(1)	-1.93	-0.07	3.68(syn)(1)	-1.75	1.11	3.25±0.08(syn)(2)	-2.18	0.24	3.70(syn)(1)	-1.73	0.61
Fe I	26	7.50	5.64±0.06(19)	-1.86	-	4.64±0.07(12)	-2.86	-	5.08±0.15(8)	-2.42	-	5.16±0.10(16)	-2.34	-
Fe II	26	7.50	5.64±0.01(2)	-1.86	-	4.64±0.13(2)	-2.86	-	5.08±0.16(2)	-2.42	-	5.16±0.07(3)	-2.34	-
Co I	27	4.99	3.01(syn)(1)	-1.98	-0.12	-	-	-	-	-	-	-	-	-
Ni I	28	6.22	4.22±0.18(4)	-2.00	-0.14	4.12±0.04(3)	-2.10	0.76	3.97±0.10(3)	-2.25	0.17	4.15±0.15(4)	-2.07	0.27
Cu I	29	4.19	-	-	-	-	-	-	-	-	-	1.40(syn)(1)	-2.81	-0.47
Zn I	30	4.56	3.00(1)	-1.56	0.30	2.33(1)	-2.23	0.63	-	-	-	-	-	-
Rb I	37	2.52	0.75(syn)(1)	-1.77	0.09	0.72(syn)(1)	-1.80	1.06	-	-	-	-	-	-
Sr I <sub>NLTE</sub>	38	2.87	3.07(syn)(1)	0.20	2.06	-	-	-	-	-	-	-	-	-
Y I	39	2.21	2.43(syn)(1)	0.22	2.08	-	-	-	-	-	-	-	-	-
Y II	39	2.21	2.71±0.13(3)	0.50	2.36	0.38±0.10(2)	-1.83	1.03	0.58±0.08(4)	-1.63	0.79	0.75±0.12(2)	-1.46	0.88
Zr I	40	2.58	2.88(syn)(1)	0.30	2.16	1.03±0.10(2)	-1.55	1.31	-	-	-	1.77±0.03(2)	-0.81	1.53
Zr II	40	2.58	2.29±0.07(2)	-0.29	1.57	0.78(syn)(1)	-1.80	1.06	1.20(syn)(1)	-1.38	1.04	1.32(syn)(1)	-1.26	1.08
Ba I <sub>NLTE</sub>	56	2.18	2.66(syn)(1)	0.48	2.34	1.03(syn)(1)	-1.15	1.71	1.50(syn)(2)	-0.68	1.74	1.42±0.05(syn)(1)	-0.76	1.58
Ba II <sub>NLTE</sub>	56	2.18	2.58(syn)(1)	0.40	2.26	-	-	-	1.51(syn)(1)	-0.67	1.75	-	-	-
La II	57	1.10	1.90(syn)(2)	0.80	2.66	0.22(syn)(1)	-0.88	1.98	-	-	-	0.30(syn)(2)	-0.80	1.54
Ce II	58	1.58	2.20±0.13(3)	0.62	2.48	0.63±0.13(4)	-0.95	1.91	1.00±0.14(4)	-0.58	1.84	0.75±0.12(2)	-0.83	1.51
Pr II	59	0.72	1.43±0.11(3)	0.71	2.57	-0.14±0.12(2)	-0.86	2.00	0.18±0.11(4)	-0.54	1.88	-0.06(1)	-0.90	1.44
Nd II	60	1.42	2.20±0.14(6)	0.78	2.64	0.53±0.13(6)	-0.89	1.97	0.99±0.14(13)	-0.43	1.99	0.69±0.03(2)	-0.73	1.61
Sm II	62	2.41	1.17±0.11(6)	0.21	2.07	0.19±0.02(3)	-0.77	2.09	0.59±0.19(2)	-0.37	2.05	0.06±0.02(2)	-0.90	1.44
Eu I <sub>NLTE</sub>	63	0.52	-0.05(syn)(1)	-0.57	1.29	-1.02(syn)(1)	-1.54	1.32	-0.62(syn)(1)	-1.14	1.28	-0.70(syn)(1)	-1.22	1.12

\* Asplund et al. (2009), The number of lines used for abundance determination are given within the parenthesis.

Except HE 1354–2257, all other stars show  $[N/Fe]>1$ . Once the carbon, nitrogen, and oxygen abundances are derived, we re-derived the oxygen abundance. Then with this oxygen abundance carbon and then nitrogen abundances are re-estimated. This iterative process is done until a convergence is obtained.

The <sup>12</sup>CN lines at 8003.292, 8003.553, 8003.910 Å, and <sup>13</sup>CN lines at 8004.554, 8004.728, 8004.781 Å are used to derive the carbon isotopic ratio, <sup>12</sup>C/<sup>13</sup>C in the HSEP spectra of the stars that cover these regions. The SUBARU spectra used for three objects, however extend only till 6800 Å in the wavelength region. The values obtained for this ratio in BD–19 132, BD–19 290, BD+19 3109, and HD 202851 are 18, 4, 9, and 42 respectively. These estimates are consistent with what is expected from the evolutionary stages of the program stars and also consistent with the values in the range 2.5 - 40 (Bisterzo et al. 2011) for CEMP-s and CEMP-r/s stars.

The equivalent width measurement of several lines listed in Table A2 are used to derive the abundance of Na, Mg, Si, Ca, Ti, Cr, Ni, and Zn. We could not estimate sodium abundance in HE 1157–0518. The star HE 1304–2111 shows the largest enhancement of Na with  $[Na/Fe]\sim 2.83$ . The lines used to derive the Na abundance in this star were very strong, so this abundance may not be reliable. The NLTE corrections of these lines were not available. The stars, BD–19 132 and BD–19 290 have  $[Na/Fe]>1$ . The

Mg abundance of the program stars are in the range  $-0.02\leq[Mg/Fe]\leq 0.61$ , similar to that observed in the normal stars in the Galaxy (Figure 5).

The elements Sc, V, Mn, Co, and Cu show HFS. The abundances of these elements are derived using the spectral synthesis calculation, taking the hyper-fine components into account. The hyper-fine components of these elements are taken from Prochaska & McWilliam (2000) and Prochaska et al. (2000). Sc abundance is derived mainly from the Sc II lines at 6245.637, 6309.920, and 6604.601 Å. It shows solar value in the star HE 1354–2257, while it is enhanced in all other stars with values ranging from 0.53 to 0.81. Spectral synthesis calculation of the V I lines at 4864.731, 5727.048, and 6251.827 Å are used to derive the vanadium abundance. Three objects in our sample, BD–19 290, HE 1304–2111, and HE 1354–2257 show  $[V/Fe]>1$ , whereas it is slightly under-abundant in HD 202851 and near-solar in the other stars. The Mn abundance is estimated from the Mn I lines at 4761.530, 6013.513, and 6021.89 Å. We have derived the Co abundance from Co I lines at 5342.695, and 5483.344 Å and Cu abundance from Cu I line at 5105.537 Å. In the case of BD+19 3109, cobalt abundance is derived from the lines Co I 4792.846, 4867.872, and 4792.846 Å. A comparison of the light element abundances observed in our program stars with their counterparts in normal stars and other classes of chemically peculiar stars are shown in Figure 5. While the estimated abundances of the elements

**Table 5.** Elemental abundances in HE 1354–2257, BD+19 3109, and HD 202851

	Z	HE 1354–2257				BD+19 3109			HD 202851		
		solar $\log \epsilon^*$	$\log \epsilon$	[X/H]	[X/Fe]	$\log \epsilon$	[X/H]	[X/Fe]	$\log \epsilon$	[X/H]	[X/Fe]
C (C <sub>2</sub> band 5165 Å)	6	8.43	8.40(syn)	−0.03	2.08	8.69	0.26	2.49	8.30(syn)	−0.13	0.72
C (C <sub>2</sub> band 5635 Å)	6	8.43	8.30(syn)	−0.13	1.98	8.65	0.22	2.45	8.45(syn)	0.02	0.87
<sup>12</sup> C/ <sup>13</sup> C	–	–	–	–	–	–	–	9	–	–	42
N	7	7.83	6.23(syn)	−1.60	0.51	7.83(syn)(3)	0.00	2.23	8.40±0.02(syn)(3)	−0.57	1.42
O	8	8.69	7.09(syn)(1)	−1.60	0.51	–	–	–	8.19(syn)(1)	−0.50	0.35
Na I	11	6.24	4.71±0.06(2)	−1.53	0.58	4.13±0.02(2)	−2.11	0.12	5.92±0.08(3)	−0.32	0.53
Mg I	12	7.60	5.47(1)	−2.13	−0.02	6.13±0.14(3)	−1.47	0.76	7.02±0.10(2)	−0.58	0.27
Si I	14	7.51	5.89±0.16(2)	−1.62	0.49	–	–	–	6.63(1)	−0.88	−0.03
Ca I	20	6.34	4.45±0.13(7)	−1.89	0.22	4.20±0.11(7)	−2.14	0.09	5.46±0.14(8)	−0.88	−0.03
Sc II	21	3.15	1.05(syn)(1)	−2.10	0.01	1.45(syn)(1)	−1.70	0.53	2.86(syn)(1)	−0.29	0.56
Ti I	22	4.95	2.60(1)	−2.35	−0.24	3.45±0.10(6)	−1.50	0.73	4.37±0.15(13)	−0.58	0.27
Ti II	22	4.95	2.70±0.07(4)	−2.25	−0.14	3.14±0.13(5)	−1.81	0.42	4.40±0.17(9)	−0.55	0.30
V I	23	3.93	2.95(syn)(2)	−0.98	1.13	1.83(syn)(1)	−2.10	0.13	2.75(syn)(1)	−1.18	−0.33
Cr I	24	5.64	–	–	–	2.83±0.09(7)	−2.81	−0.58	5.25±0.13(9)	−0.39	0.46
Cr II	24	5.64	4.30±0.08(2)	−1.34	0.77	–	–	–	5.20±0.19(3)	−0.44	0.41
Mn I	25	5.43	3.59(syn)(1)	−1.84	0.27	3.13(syn)(2)	−2.30	−0.07	4.71(syn)(1)	−0.72	0.13
Fe I	26	7.50	5.39±0.17(20)	−2.11	–	5.27±0.09(27)	−2.23	–	6.65±0.01(30)	−0.85	–
Fe II	26	7.50	5.39±0.15(4)	−2.11	–	5.27±0.02(3)	−2.23	–	6.65±0.07(3)	−0.85	–
Co I	27	4.99	3.59(syn)(1)	−1.40	0.71	3.20±0.07(3)	−1.79	0.44	4.30(syn)(1)	−0.69	0.16
Ni I	28	6.22	3.81±0.20(3)	−2.41	−0.30	4.46±0.12(3)	−1.76	0.47	5.80±0.12(11)	−0.42	0.43
Cu I	29	4.19	–	–	–	–	–	–	2.85(syn)(1)	−1.34	−0.49
Zn I	30	4.56	2.50(1)	−2.06	0.05	2.48(1)	−2.08	0.15	3.48(1)	−1.08	−0.23
Rb I	37	2.52	–	–	–	0.20(syn)(1)	−2.32	−0.09	1.49(syn)(1)	−1.03	−0.18
Sr I <sub>NLTE</sub>	38	2.87	2.44(syn)(1)	−0.43	1.68	–	–	–	3.12(syn)(1)	0.25	1.10
Y I	39	2.21	2.18(syn)(1)	−0.03	2.08	1.16(syn)(1)	−1.05	1.18	2.44(syn)(1)	0.23	1.08
Y II	39	2.21	–	–	–	1.42±0.16(3)	−0.79	1.44	3.05±0.08(4)	0.84	1.69
Zr I	40	2.58	2.27(syn)(1)	−0.37	1.80	0.98(syn)(1)	−1.60	0.63	3.50(syn)(1)	0.92	1.77
Zr II	40	2.58	–	–	–	1.28(1)(1)	−1.30	0.93	3.79(syn)(1)	1.21	2.06
Ba II <sub>LTE</sub>	56	2.18	1.70(syn)(2)	−0.48	1.63	1.68(syn)(1)	−0.60	1.73	3.50(syn)(1)	1.32	2.17
Ba II <sub>NLTE</sub>	56	2.18	–	–	–	–	–	–	3.15(syn)(1)	0.97	1.82
La II	57	1.10	0.40(syn)(1)	−0.70	1.41	0.50(syn)(1)	−0.60	1.63	1.85(syn)(2)	0.75	1.60
Ce II	58	1.58	1.17±0.07(4)	−0.41	1.70	0.92±0.11(7)	−0.66	1.57	2.62±0.14(8)	1.04	1.89
Pr II	59	0.72	0.14±0.09(3)	−0.58	1.53	0.23±0.12(4)	−0.49	1.74	2.04±0.14(4)	1.32	2.17
Nd II	60	1.42	0.98±0.13(9)	−0.44	1.67	0.82±0.09(14)	−0.60	1.63	2.38±0.11(9)	0.96	1.81
Sm II	62	2.41	0.50±0.08(3)	−0.46	1.65	0.38±0.11(8)	−0.58	1.65	1.83±0.09(6)	0.87	1.72
Eu II <sub>LTE</sub>	63	0.52	−1.12(syn)(1)	−1.64	0.47	−0.99(syn)(1)	−1.51	0.72	0.56(syn)(1)	0.04	0.89
Eu II <sub>NLTE</sub>	63	0.52	−1.16(syn)(1)	−1.68	0.43	–	–	–	–	–	–

\* Asplund et al. (2009), The number of lines used for abundance determination are given within the parenthesis.

Mg, Si, Ca, Sc, Ti, Co, Ni, and Zn in all the program stars follow the Galactic trend (similar to that observed in normal stars), Na, V, Cr, and Mn are enhanced in a few program stars. Such enhancements of Na and Fe-peak elements are observed in a few CEMP stars such as HE 1327–2326 (Aoki et al. 2006; Frebel et al. 2008) and SMSS J031300.36–670839.3 (Bessell et al. 2015). The models of spinstar (Maeder et al. 2015; Maeder & Meynet 2015), faint SNe (Iwamoto et al. 2005; Tominaga et al. 2007; Bessell et al. 2015) have been used to reproduce their observed abundance pattern. According to Aoki et al. (2006), either faint SNe or AGB-binary mass transfer along with the accretion of metals from ISM might explain the observed abundance pattern of HE 1327–2326. Choplin et al. (2017) have suggested that spinstar could also have played a role in the formation of some CEMP-s stars and the abundance patterns of CEMP-s stars may be resulting from several sources. From these facts, the observed enhanced abundances of Na, V, Cr, and Mn in the program stars BD–19 290, HE 1304–2111 and HE 1354–2257 may be attributed to the pre-enriched ISM from which they

were formed. Also, some of the CEMP-(s&t/s) stars show enhanced abundances of Na at low metallicities (Bisterzo et al. 2011 and references therein, Allen et al. 2012, Karinkuzhi et al. 2021). A discussion on the Na abundance is provided in section 8.3.

## 4.2. Heavy elements

### 4.2.1. The light s-process elements: Rb, Sr, Y, Zr

The spectral synthesis calculation of Rb I 7800.259 Å resonance line is used to derive the rubidium abundance in the program stars, by taking the hyper-fine components from Lambert & Luck (1976). Rb I 7947.597 Å was blended and could not be used for the abundance determination. We could determine Rb abundance only in the stars whose spectra are from HCT/HESP. It is enhanced in BD–19 290 with [Rb/Fe]>1, shows near-solar value in other three stars: BD–19 132, BD+19 3109, and HD 202851.

Strontium abundance is derived from the spectral synthesis calculation of Sr I 4607.327 Å line with log *g<sub>f</sub>* value taken from Bergemann et al. (2012). We could estimate strontium abundance only in three objects;

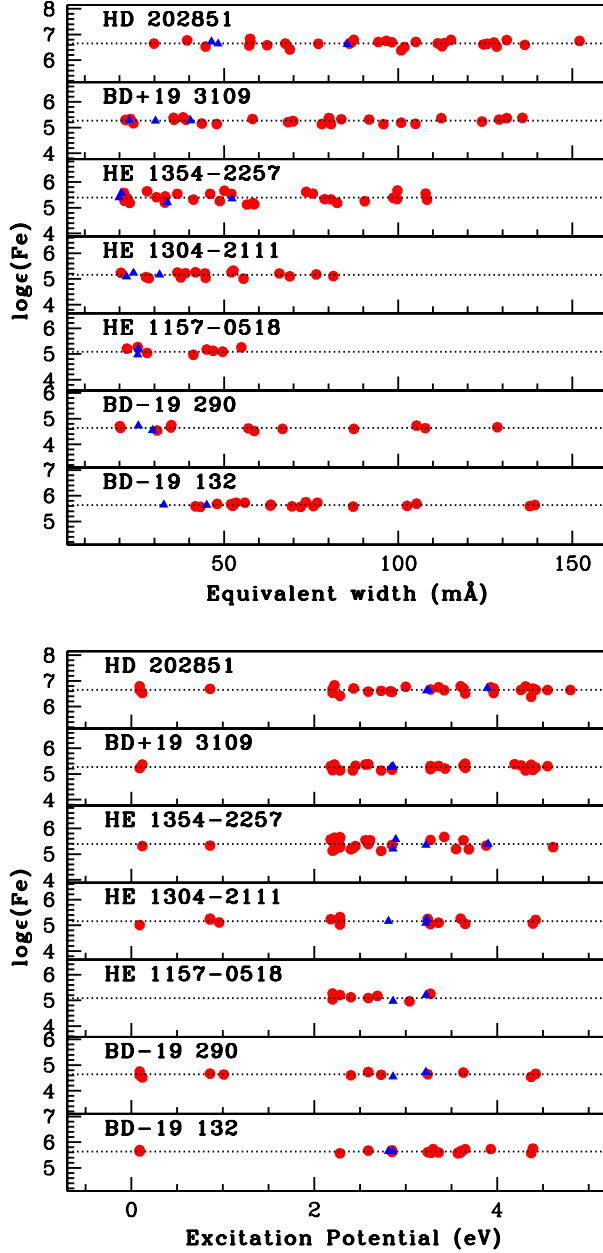


**Figure 2.** Iron abundances of the program stars derived from individual Fe I and Fe II lines as function of excitation potential (lower panel), and equivalent width (upper panel). The dotted lines correspond to the derived and adopted Fe abundance for each star. Solid circles correspond to Fe I and solid triangles correspond to Fe II lines.

BD-19 132, HE 1354-2257, and HD 202851 and they show  $[\text{Sr}/\text{Fe}] > 1$ . It has been proven that the Sr I lines are affected by NLTE effects (Barklem & O'Mara 2000; Short & Hauschildt 2006). The NLTE corrections of Sr I 4607.327 Å line is adopted from Bergemann et al. (2012). They have calculated the NLTE corrections for

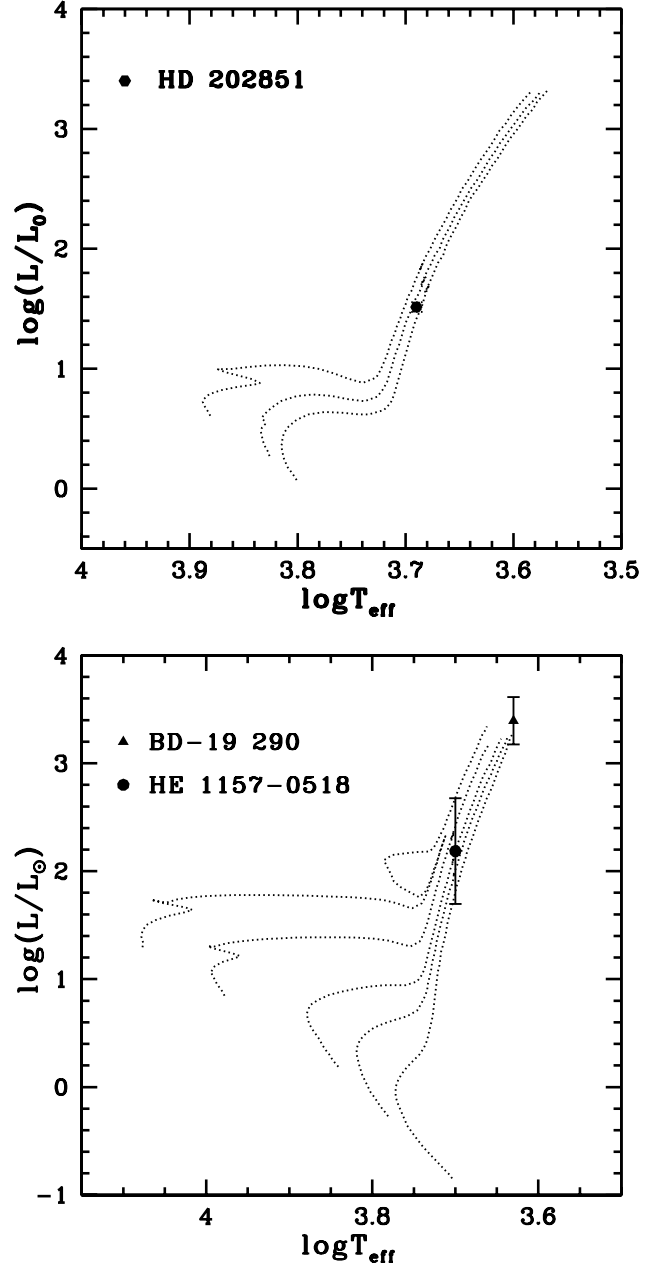


**Figure 3.** The evolutionary tracks for 1.0, 1.1, and 1.2  $M_{\odot}$  for  $z = 0.004$  (upper panel) and for 0.6, 0.8, 1.0, 1.4, and 1.8  $M_{\odot}$  for  $z = 0.004$  (lower panel) are shown from bottom to top.

different combinations of stellar atmospheric parameters for four different stars. For the star HD 122563, the NLTE correction is +0.47 dex, which has got similar atmospheric parameters ( $T_{\text{eff}} = 4600$  K,  $\log g = 1.60$ ,  $\zeta = 1.80$  km s $^{-1}$ ,  $[\text{Fe}/\text{H}] = -2.50$ ) as BD-19 132 and HE 1354-2257. For these two stars, we have applied this correction term to our estimated abundance of Sr. For the star HD 202851, the NLTE correction ( $\sim +0.32$  dex)

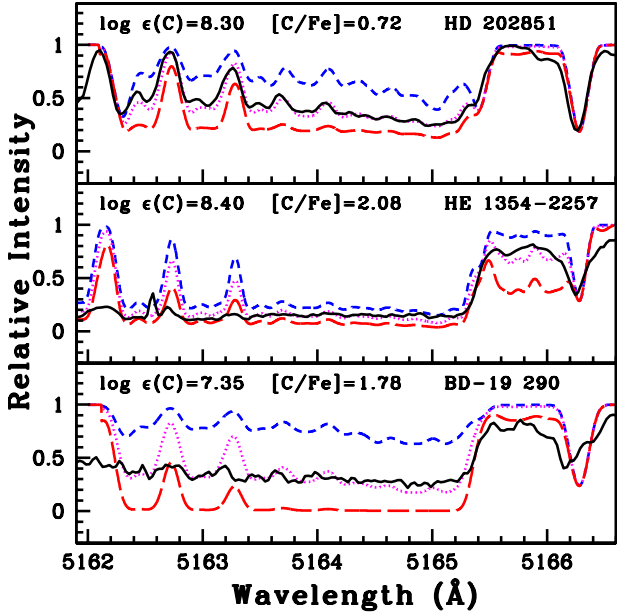
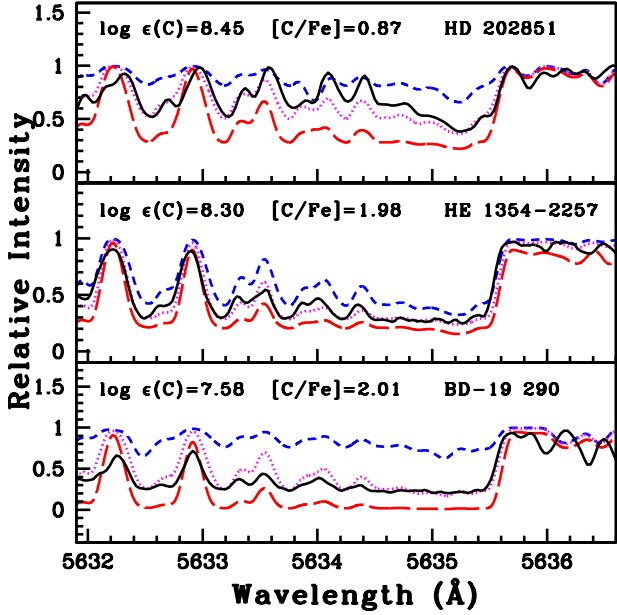


**Figure 4.** Synthesis of C<sub>2</sub> band around 5165 Å (lower panel) and 5635 Å (upper panel). Dotted and solid lines represent synthesized and observed spectra respectively. Short dashed and long dashed lines represent the synthetic spectra for  $\Delta$  [C/Fe] =  $-0.3$  and  $+0.3$  respectively.

has been taken from the Table 3 of Bergemann et al. (2012) which corresponds to a similar combination of atmospheric parameters as HD 202851. The spectrum synthesis fit for Sr I 4607.327 Å line for the program stars are shown in Figure 6

The yttrium abundance is derived from Y I 6435.004 Å line and the equivalent width measurement of the

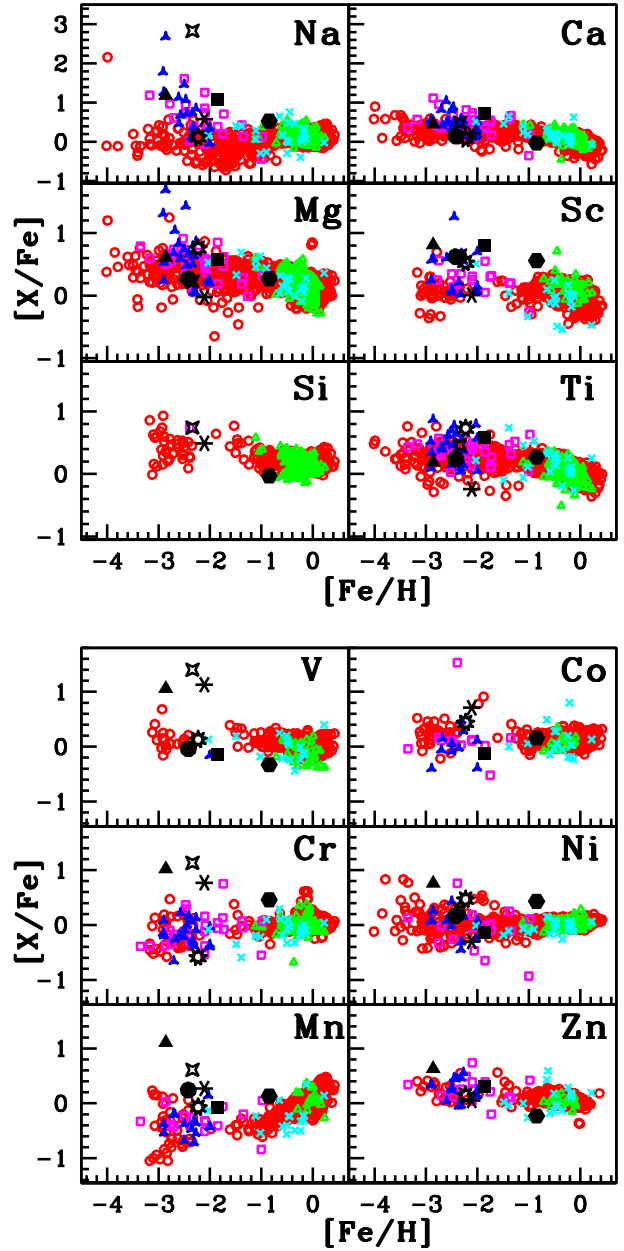


**Figure 5.** Observed [X/Fe] ratios of the light elements in the program stars with respect to metallicity [Fe/H]. Red open circles correspond to normal giants from literature (Honda et al. 2004; Venn et al. 2004; Aoki et al. 2005, 2007; Reddy et al. 2006; Luck & Heiter 2007; Hansen et al. 2016a; Yoon et al. 2016). Magenta open squares and blue starred triangles represent CEMP-s and CEMP-r/s stars respectively from literature (Masseron et al. 2010; Purandardas et al. 2019; Karinkuzhi et al. 2021; Shejeelammal et al. 2021). Cyan crosses represent CH stars from literature (Vanture 1992; Karinkuzhi & Goswami 2014, 2015; Goswami et al. 2016; Shejeelammal et al. 2021). Green open triangles are Ba stars from literature (Allen & Barby 2006; de Castro et al. 2016; Yang et al. 2016; Karinkuzhi et al. 2018; Shejeelammal et al. 2020). BD-19 132 (filled square), BD-19 290 (filled triangle), HE 1157-0518 (filled circle), HE 1304-2111 (four-sided star), HE 1354-2257 (six-sided cross), BD+19 3109 (nine-sided star), and HD 202851 (filled hexagon).

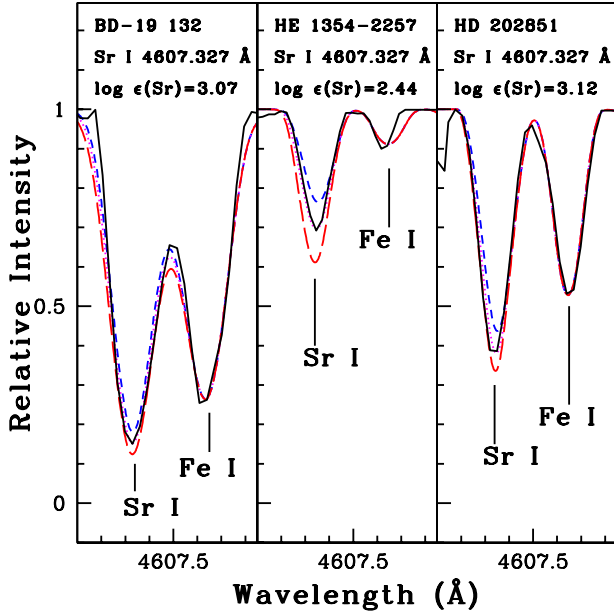


**Figure 6.** Synthesis of Sr I line at 4607.327 Å. Dotted and solid lines represent synthesized and observed spectra respectively. Short dashed and long dashed lines represent the synthetic spectra for  $\Delta[\text{Sr}/\text{Fe}] = -0.3$  and  $+0.3$  respectively.

Y II lines listed in Table A2. We could not estimate Y I abundances in BD-19 290, HE 1157-0518, and HE 1304-2111 and Y II abundance in HE 1354-2257 as no good lines are detected in their spectra due to these species. The abundance derived from Y II lines are higher than that estimated from Y I lines wherever we could use both the species. It is enhanced in all the program stars with  $[\text{X}/\text{Fe}] \geq 0.79$ . The zirconium abundance is estimated using the spectral synthesis calculation of Zr I 6134.585 Å and Zr II 5112.297 Å and equivalent width measurement of several Zr I and Zr II lines whenever available. We could not estimate Zr I abundance in HE 1157-0518 and Zr II abundance in HE 1354-2257. The abundance estimated from Zr I lines are in the range 0.63 - 2.16 and that from Zr II lines are in the range 0.93 - 2.06.

#### 4.2.2. The heavy s-process elements: Ba, La, Ce, Pr, Nd

The barium abundance is derived from the spectral synthesis calculation of Ba II 5853.668 Å line in BD-19 132, HE 1157-0518, and HD 202851. This line is blended in all other stars and could not be used for abundance determination. This line is known to be affected by NLTE effect. The NLTE correction to the abundance derived from this line is adopted from Andrievsky et al. (2009), which are +0.22, +0.41, and +0.35 dex re-

spectively for the above objects. The Ba II 6141.713, 4934.076, and 6496.897 Å lines are also used for the estimation of Ba abundance. The line list for Ba II 6496.897 Å line is taken from linemake<sup>2</sup> atomic and molecular line database (Placco et al. 2021). The hyper-fine components of other lines are taken from McWilliam (1998). Barium is enhanced in all the program stars with  $[\text{Ba}/\text{Fe}] > 1$ . The spectral synthesis fits for Ba II 5853.668 and 6141.713 Å lines are shown in Figure 7.

Spectral synthesis calculation of La II 4748.726, 5259.379, 4921.776, 5301.969, 5303.528 Å lines, whenever available, is used to derive the abundance of lanthanum in the program stars. The hyper-fine components of La II 4921.776 Å line are taken from Jonsell et al. (2006) and 5301.969, 5303.528 Å lines from Lawler et al. (2001), whereas it is not available for 4748.726 and 5259.379 Å lines. We could not find any useful lines due to La in the star HE 1157-0518 for abundance determination. In all other stars it is enhanced with  $[\text{La}/\text{Fe}] \geq 1.41$  with BD-19 132 showing the highest enhancement of  $[\text{La}/\text{Fe}] \sim 2.66$ . Equivalent width measurement of several spectral lines were used to derive the abundances of Ce, Pr, and Nd. All these elements are enhanced in all our program stars with  $[\text{X}/\text{Fe}] > 1.40$ .

Finally, the  $[\text{ls}/\text{Fe}]$ ,  $[\text{hs}/\text{Fe}]$ , and  $[\text{hs}/\text{ls}]$  ratios of the program stars are estimated, where ls is the light s-process elements; Sr, Y, and Zr and hs is the heavy s-process elements; Ba, La, Ce, and Nd. We have also estimated  $[\text{s}/\text{Fe}]$  ratio, an indicator of total s-process content of the star (s refers to the s-process elements Sr, Y, Zr, Ba, La, Ce, and Nd). The neutron-density dependent  $[\text{Rb}/\text{Zr}]$  ratio is also estimated. The values for these ratios are given in Table 6. These ratios are discussed in section 8.

#### 4.2.3. The r-process elements: Sm, Eu

The abundance of samarium is derived from the equivalent width measurement of Sm II lines listed in Table A2. The  $[\text{Sm}/\text{Fe}]$  values in our program stars are in the range 1.44 - 2.09. The europium abundance is derived from the spectral synthesis calculation of Eu II 6645.064 Å line in all our program stars. In HE 1354-2257, we could use Eu II 4129.725 Å line also. In all other program stars, this line is not usable for abundance determination. This line shows NLTE effect and the appropriate correction ( $\sim +0.16$ ) has been adopted from

<sup>2</sup> linemake contains laboratory atomic data (transition probabilities, hyperfine and isotopic substructures) published by the Wisconsin Atomic Physics and the Old Dominion Molecular Physics groups. These lists and accompanying line list assembly software have been developed by C. Sneden and are curated by V. Placco at <https://github.com/vmplacco/linemake>.

**Table 6.** Estimates of [ls/Fe], [hs/Fe], [s/Fe], [hs/ls], [Rb/Zr]

Star name	[Fe/H]	[ls/Fe]	[hs/Fe]	[s/Fe]	[hs/ls]	[Rb/Zr]
BD-19 132	-1.86	1.38	2.52	2.34	1.14	-2.07
BD-19 290	-2.86	1.05	1.89	1.61	0.84	-0.25
HE 1157-0518	-2.42	1.27	1.86	1.37	0.59	-
HE 1304-2111	-2.34	0.98	1.56	1.37	0.58	-
HE 1354-2257	-2.11	1.85	1.61	1.71	-0.24	-
BD+19 3109	-2.23	0.91	1.64	1.40	0.73	-0.72
HD 202851	-0.85	1.31	1.83	1.61	0.52	-1.95

Mashonkina et al. (2008). None of the stars has good Eu II 6437.640 Å line usable for abundance determination. The hyper-fine components of Eu are taken from Worley et al. (2013). All the stars show enhancement of Eu with [Eu/Fe]>0.7 except the star HE 1354-2257 where it is moderately enhanced with [Eu/Fe]~0.47. The spectral synthesis fits for Eu II 6645.064 Å line are shown in Figure 8.

In Tables 4 ad 5, the abundances derived from the lines showing NLTE effect are given separately after the NLTE correction. Figure 9 shows a comparison of the observed abundances of heavy elements in our program stars with their counterparts in normal stars and other chemically peculiar stars. From the figure, it is clear that our program stars show clear over-abundance of heavy elements with respect to the normal stars. A comparison of the elemental abundances in the program stars with the literature value is given in Table 7.

### 5. ABUNDANCE UNCERTAINTIES

The uncertainties on the abundances of all the elements, logϵ, are calculated following the detailed procedure in Shejeelammal et al. (2020).

The uncertainty in the abundance of an element is given by;

$$\sigma_{\log\epsilon}^2 = \sigma_{ran}^2 + \left(\frac{\partial \log\epsilon}{\partial T}\right)^2 \sigma_{T_{eff}}^2 + \left(\frac{\partial \log\epsilon}{\partial \log g}\right)^2 \sigma_{\log g}^2 + \left(\frac{\partial \log\epsilon}{\partial \zeta}\right)^2 \sigma_{\zeta}^2 + \left(\frac{\partial \log\epsilon}{\partial [Fe/H]}\right)^2 \sigma_{[Fe/H]}^2$$

where  $\Delta T_{eff} \sim \pm 100$  K,  $\Delta \log g \sim \pm 0.2$  dex,  $\Delta \zeta \sim \pm 0.2$  km s<sup>-1</sup>, and  $\Delta [Fe/H] \sim \pm 0.1$  dex are the typical uncertainties in the atmospheric parameters. The  $\sigma_{ran} = \frac{\sigma_s}{\sqrt{N}}$ , is the random error in the elemental abundance which arises from the line-to-line scatter (standard deviation,  $\sigma_s$ ) of the abundances of a particular element species derived from N number of lines. Finally, total uncertainty in [X/Fe] is calculated by;

$$\sigma_{[X/Fe]}^2 = \sigma_X^2 + \sigma_{Fe}^2.$$

In order to simplify the calculation, we made the assumption that the uncertainties due to different parameters are independent, following de Castro et al. (2016),

Karinkuzhi et al. (2018), Cseh et al. (2018). However, since most of the stellar atmospheric parameters are correlated, our estimates are to be taken as upper limits. The differential abundances,  $\Delta \log \epsilon$ , for the variations in each stellar atmospheric parameters calculated for the star HD 202851 is given in Table 8.

### 6. KINEMATIC ANALYSIS

It is equally as important as the chemical composition of a star to understand its kinematics and the Galactic population to which it belongs. We have calculated the components of the spatial velocities of the program stars with respect to the Local Standard of Rest (LSR),  $U_{LSR}$ ,  $V_{LSR}$ , and  $W_{LSR}$ , following the procedures discussed in Johnson & Soderblom (1987) and Bensby et al. (2003).

The spatial velocity components with respect to the LSR is given by;

$$(U, V, W)_{LSR} = (U, V, W) + (U, V, W)_{\odot} \text{ km/s.}$$

$(U, V, W)_{\odot} = (11.1, 12.2, 7.3)$  km/s is the solar motion with respect to LSR (Schönrich et al. 2010). Total space velocity is calculated as;

$$V_{spa}^2 = U_{LSR}^2 + V_{LSR}^2 + W_{LSR}^2.$$

The membership of the stars to each Galactic population is determined following the probability calculations given in Mishenina et al. (2004), Bensby et al. (2003, 2004), and Reddy et al. (2006). The proper motions in RA and DEC ( $\mu_{\alpha}$  and  $\mu_{\delta}$ ), parallax ( $\pi$ ) are taken from SIMBAD astronomical database and Gaia DR2 (Gaia Collaboration et al. 2018, <https://gea.esac.esa.int/archive/>). The detailed procedure can be found in Shejeelammal et al. (2021). The components of the spatial velocity, total space velocity and probability that a star belongs to a particular Galactic population are presented in Table 9. While the stars BD-19 290, HE 1157-0518, HE 1354-2257, and BD+19 3109 belong to the Galactic halo, BD-19 132, HE 1304-2111, and HD 202851 belong to the Galactic thin disk.

### 7. CLASSIFICATION OF THE PROGRAM STARS

**Table 7.** Comparison of the elemental abundances of our program stars with the literature values.

Star name	[Fe /H]	[C/Fe]	[N/Fe]	[Mg/Fe]	[Ca/Fe]	[Ti/Fe]	[Cr/Fe]	Ref.
HE 1157–0518	−2.42	2.31	1.52	0.27	0.15	0.06	−0.04	1
	−2.40	2.15	1.56	0.50	0.16	0.09	−0.28	2
HD 202851	−0.85	0.72	1.42	0.27	−0.03	0.30	0.46	1
	−0.70	-	-	-	-	0.00	−0.20	3

Star name	[Fe /H]	[Y/Fe]	[Ba/Fe]	[La/Fe]	[Ce/Fe]	[Nd/Fe]	Ref.
HE 1157–0518	−2.42	0.79	1.75	-	1.84	1.99	1
	−2.40	-	2.14	-	-	-	2
HD 202851	−0.85	1.08	2.00	1.60	1.89	1.81	1
	−0.70	1.30	1.60	1.40	1.30	1.60	3

References: 1. This work, 2. Aoki et al. (2007), 3. Sperauskas et al. (2016)

All the stars analyzed here are metal-poor objects with  $[\text{Fe}/\text{H}] < -1$ , except HD 202851 which has a metallicity of  $[\text{Fe}/\text{H}] \sim -0.85$ . Five objects in the sample are very metal-poor with  $[\text{Fe}/\text{H}] < -2$ . All the stars in our sample show enhanced abundance of carbon with  $[\text{C}/\text{Fe}] \geq 0.70$ . According to Beers & Christlieb (2005), the stars with  $[\text{Fe}/\text{H}] \leq -2$  and  $[\text{C}/\text{Fe}] > 1$  are Carbon Enhanced Metal-Poor (CEMP) stars. However, a number of stars with  $[\text{Fe}/\text{H}] < -1$  are identified as CEMP stars in literature (Jonsell et al. 2006; Goswami et al. 2006; Aoki et al. 2007; Goswami & Aoki 2010; Masseron et al. 2010; Abate et al. 2016; Shejeelammal et al. 2021; Karinkuzhi et al. 2021) etc.. Several authors have adopted different lower limits for  $[\text{C}/\text{Fe}]$  ratio to define the CEMP stars, for instance,  $[\text{C}/\text{Fe}] \geq 0.7$  (Carollo et al. 2012; Lee et al. 2013; Norris et al. 2013a; Skúladóttir et al. 2015),  $[\text{C}/\text{Fe}] > 0.9$  (Jonsell et al. 2006; Masseron et al. 2010),  $[\text{C}/\text{Fe}] > 1$  (Abate et al. 2016; Hansen et al. 2019). However, in the case of evolved metal-poor giants, the carbon abundance will be lower compared to their earlier evolutionary stages due to the internal mixing of the CNO processed material from the stellar interiors (Gratton et al. 2000; Spite et al. 2005, 2006; Aoki et al. 2007; Placco et al. 2014). This will be discussed in detail in the next section. So while setting the limit for the  $[\text{C}/\text{Fe}]$  ratio of CEMP stars, the evolutionary stage of the star should also be taken care of. Aoki et al. (2007) have taken into consideration the luminosity of the star, which represents the evolutionary stage, to account for the depletion of surface carbon to set a threshold  $[\text{C}/\text{Fe}]$  that defines CEMP star population. The following empirical definition is given by Aoki et al. (2007) for the CEMP stars;

- (i)  $[\text{C}/\text{Fe}] \geq +0.7$ ; if  $\log(L/L_{\odot}) \leq 2.3$
- (ii)  $[\text{C}/\text{Fe}] \geq +3.0 - \log(L/L_{\odot})$ ; if  $\log(L/L_{\odot}) > 2.3$

We have adopted this criteria to define the CEMP stars in our sample, which is demonstrated in Figure 10. It is clear from the figure that CEMP stars and non-carbon-enhanced metal-poor stars belong to two different regions of the diagram. Even though the star HD 202851 shows a  $[\text{C}/\text{Fe}]$  value that resembles CEMP stars according to this definition, because of its higher metallicity,  $[\text{Fe}/\text{H}] \sim -0.85$ , we classify it as a CH star, whereas all other six stars in our sample are CEMP stars.

There exist a number classification scheme in literature for the sub-classification of CEMP stars (Abate et al. 2016; Frebel 2018; Hansen et al. 2019), the Beers & Christlieb (2005) being the pioneering one. Beers & Christlieb (2005) and Abate et al. (2016) considered  $[\text{Ba}/\text{Fe}]$ ,  $[\text{Eu}/\text{Fe}]$ , and  $[\text{Ba}/\text{Eu}]$  ratios to define CEMP sub-classes, Hansen et al. (2019) considered  $[\text{Sr}/\text{Ba}]$  ratio, and Frebel (2018) considered  $[\text{Sr}/\text{Ba}]$ ,  $[\text{Sr}/\text{Eu}]$ ,  $[\text{Ba}/\text{Pb}]$ , and  $[\text{La}/\text{Eu}]$  ratios. Goswami et al. (2021) revisited all these classification schemes and came up with a slightly modified criteria in terms of  $[\text{Ba}/\text{Eu}]$  and  $[\text{La}/\text{Eu}]$ . We adopted this scheme to sub-classify our CEMP stars which is as follows;

- CEMP-s;  $[\text{Ba}/\text{Fe}] \geq 1$ 
  - (i)  $[\text{Eu}/\text{Fe}] < 1$ ,  $[\text{Ba}/\text{Eu}] > 0$  and/or  $[\text{La}/\text{Eu}] > 0.5$
  - (ii)  $[\text{Eu}/\text{Fe}] \geq 1$ ,  $[\text{Ba}/\text{Eu}] > 1$  and/or  $[\text{La}/\text{Eu}] > 0.7$
- CEMP-r/s;  $[\text{Ba}/\text{Fe}] \geq 1$ ,  $[\text{Eu}/\text{Fe}] \geq 1$ 
  - (i)  $0 \leq [\text{Ba}/\text{Eu}] \leq 1$  and/or  $0 \leq [\text{La}/\text{Eu}] \leq 0.7$

Figure 11 depicts this classification scheme. The regions marked as (i) and (ii) are two CEMP-s star regions corresponding to the above mentioned conditions (i) and (ii) respectively and the region marked as (iii) corresponds to CEMP-r/s stars. In this figure, the stars BD–19 290, HE 1157–0518, and HE 1304–2111 occupy the region (iii), and they are found to be CEMP-r/s stars. We could not locate the position of the star HE 1157–0518 in the  $[\text{La}/\text{Fe}]$  -  $[\text{Eu}/\text{Fe}]$  plot as La abundance could not

**Table 8.** Change in the abundances ( $\Delta \log \epsilon$ ) of different elemental species with the variations in stellar atmospheric parameters for the representative star HD 202851 (columns 2 - 5). The rms uncertainty, computed from the random error ( $\sigma_{ran}$ ) and the differential abundances given in second to fifth columns, is given in sixth column. Total uncertainty in  $[X/Fe]$  of each elemental species is given in seventh column.

Element	$\Delta T_{eff}$ ( $\pm 100$ K)	$\Delta \log g$ ( $\pm 0.2$ dex)	$\Delta \zeta$ ( $\pm 0.2$ kms $^{-1}$ )	$\Delta [Fe/H]$ ( $\pm 0.1$ dex)	$(\Sigma \sigma_i^2)^{1/2}$	$\sigma_{[X/Fe]}$
C	$\pm 0.07$	$\pm 0.10$	$\mp 0.10$	$\pm 0.10$	0.19	0.24
N	$\pm 0.13$	$\pm 0.03$	0.00	$\pm 0.02$	0.14	0.20
O	0.00	$\pm 0.04$	$\pm 0.02$	0.00	0.05	0.15
Na I	$\pm 0.06$	$\mp 0.02$	$\mp 0.06$	$\mp 0.01$	0.10	0.17
Mg I	$\pm 0.07$	$\mp 0.06$	$\mp 0.07$	$\pm 0.01$	0.10	0.17
Si I	$\pm 0.01$	$\mp 0.01$	$\mp 0.07$	$\pm 0.01$	0.07	0.16
Ca I	$\pm 0.09$	$\mp 0.02$	$\mp 0.09$	$\mp 0.01$	0.14	0.20
Sc II	$\mp 0.03$	$\pm 0.08$	$\mp 0.10$	$\pm 0.03$	0.14	0.21
Ti I	$\pm 0.13$	$\mp 0.01$	$\mp 0.07$	$\mp 0.02$	0.16	0.21
Ti II	$\mp 0.01$	$\pm 0.07$	$\mp 0.11$	$\pm 0.03$	0.15	0.21
V I	$\pm 0.15$	$\mp 0.01$	$\mp 0.04$	$\mp 0.02$	0.16	0.21
Cr I	$\pm 0.12$	$\mp 0.01$	$\mp 0.09$	$\mp 0.01$	0.16	0.21
Cr II	$\mp 0.07$	$\pm 0.08$	$\mp 0.03$	$\pm 0.02$	0.16	0.22
Mn I	$\pm 0.10$	$\mp 0.03$	$\mp 0.13$	$\mp 0.01$	0.17	0.22
Fe I	$\pm 0.09$	$\pm 0.01$	$\mp 0.11$	0.00	0.14	–
Fe II	$\mp 0.09$	$\pm 0.09$	$\mp 0.07$	$\pm 0.05$	0.16	–
Co I	$\pm 0.09$	$\pm 0.01$	$\mp 0.03$	0.00	0.10	0.17
Ni I	$\pm 0.07$	$\pm 0.01$	$\mp 0.08$	0.00	0.11	0.18
Cu I	$\pm 0.14$	$\mp 0.01$	$\mp 0.18$	$\mp 0.01$	0.23	0.27
Zn I	$\mp 0.04$	$\pm 0.05$	$\mp 0.09$	$\pm 0.02$	0.11	0.18
Rb I	$\pm 0.10$	0.00	$\mp 0.03$	0.00	0.11	0.18
Sr I	$\pm 0.14$	$\mp 0.02$	$\mp 0.16$	$\pm 0.02$	0.22	0.26
Y I	$\pm 0.16$	0.00	$\mp 0.01$	$\mp 0.01$	0.16	0.22
Y II	0.00	$\pm 0.05$	$\mp 0.14$	$\pm 0.03$	0.16	0.22
Zr I	$\pm 0.11$	$\mp 0.01$	$\mp 0.10$	$\mp 0.02$	0.15	0.21
Zr II	$\mp 0.01$	$\pm 0.06$	$\mp 0.19$	$\pm 0.02$	0.20	0.26
Ba II	$\pm 0.03$	$\pm 0.02$	$\mp 0.07$	$\pm 0.05$	0.10	0.19
La II	$\pm 0.02$	$\pm 0.08$	$\mp 0.09$	$\pm 0.03$	0.13	0.20
Ce II	$\pm 0.01$	$\pm 0.07$	$\mp 0.13$	$\pm 0.03$	0.16	0.22
Pr II	$\pm 0.02$	$\pm 0.08$	$\mp 0.11$	$\pm 0.03$	0.16	0.22
Nd II	$\pm 0.02$	$\pm 0.07$	$\mp 0.14$	$\pm 0.03$	0.16	0.23
Sm II	$\pm 0.01$	$\pm 0.08$	$\mp 0.08$	$\pm 0.03$	0.12	0.20
Eu II	$\mp 0.02$	$\pm 0.08$	$\mp 0.02$	$\pm 0.03$	0.09	0.18

**Table 9.** Estimates of spatial velocity and probabilities for the membership to the Galactic population of the program stars

Star name	$U_{LSR}$ (kms $^{-1}$ )	$V_{LSR}$ (kms $^{-1}$ )	$W_{LSR}$ (kms $^{-1}$ )	$V_{spa}$ (kms $^{-1}$ )	$P_{thin}$	$P_{thick}$	$P_{halo}$
BD–19 132	13.66 $\pm$ 1.06	–69.13 $\pm$ 12.91	–6.75 $\pm$ 1.79	70.79 $\pm$ 12.56	0.90	0.10	0.00
BD–19 290	–252.60 $\pm$ 68.56	–573.19 $\pm$ 168.57	–38.00 $\pm$ 16.68	627.56 $\pm$ 182.56	0.00	0.00	1.00
HE 1157–0518	–113.96 $\pm$ 69.93	–449.47 $\pm$ 202.19	–154.28 $\pm$ 130.96	488.68 $\pm$ 241.24	0.00	0.00	1.00
HE 1304–2111	2.68 $\pm$ 0.18	–41.47 $\pm$ 0.25	–32.03 $\pm$ 0.27	52.47 $\pm$ 0.35	0.92	0.08	0.00
HE 1354–2257	–695.99 $\pm$ 3045.67	–1855.03 $\pm$ 5913.33	–295.05 $\pm$ 1636.19	2003.14 $\pm$ 4853.64	0.00	0.00	1.00
BD+19 3109	–122.65 $\pm$ 1.87	–253.64 $\pm$ 13.83	41.66 $\pm$ 11.43	284.80 $\pm$ 11.44	0.00	0.01	0.99
HD 202851	64.35 $\pm$ 1.90	–38.17 $\pm$ 2.92	–40.82 $\pm$ 1.68	85.23 $\pm$ 0.68	0.72	0.28	0.00

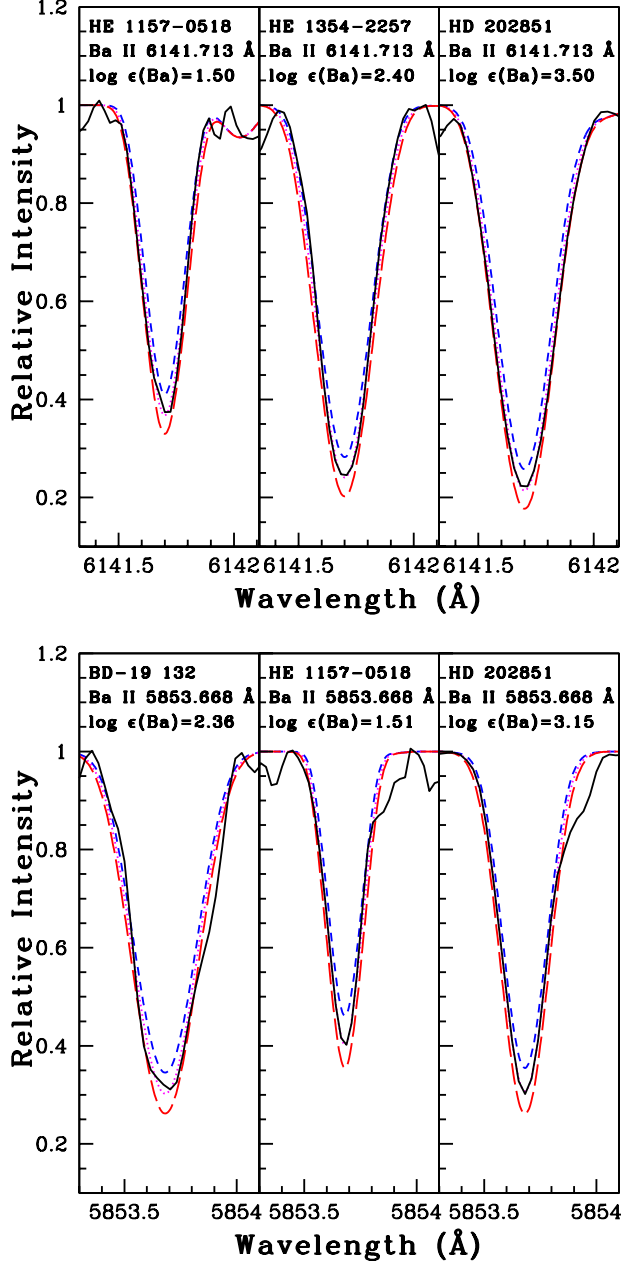


**Figure 7.** Synthesis of Ba II 5853.668 Å (lower panel) and 6141.713 Å (upper panel) lines. Dotted and solid lines represent synthesized and observed spectra respectively. Short dashed and long dashed lines represent the synthetic spectra for  $\Delta$  [Ba/Fe] =  $-0.3$  and  $+0.3$  respectively.

be estimated in this star. The objects HE 1354–2257 and BD+19 3109 clearly lie in the region (i) in both the panels and they are CEMP-s stars. The star BD–19 132 lies marginally in region (ii) in the [Ba/Fe] - [Eu/Fe] plot, but it clearly lies in the region (ii) in the [La/Fe] - [Eu/Fe] plot; hence it is identified as a CEMP-s star.

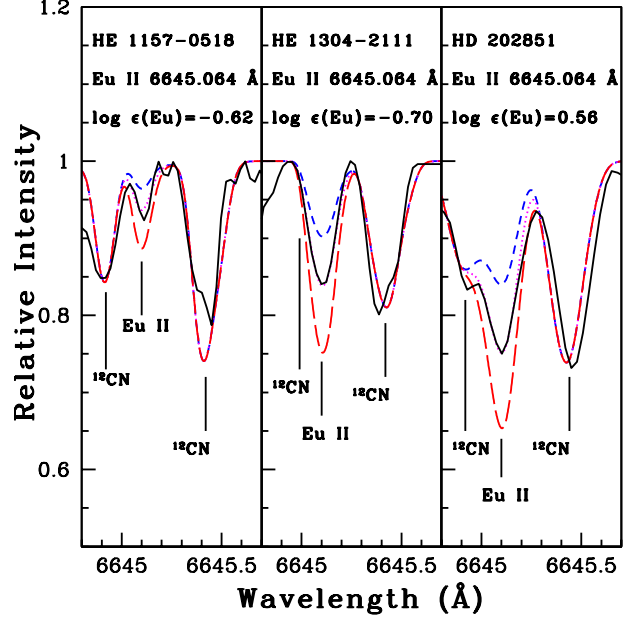


**Figure 8.** Synthesis of Eu II 6645.064 Å line. Dotted and solid lines represent synthesized and observed spectra respectively. Short dashed and long dashed lines represent the synthetic spectra for  $\Delta$  [Eu/Fe] =  $-0.3$  and  $+0.3$  respectively.

The estimated [Ba/Eu], [La/Eu] ratios of the program stars are given in Table 10.

## 8. ABUNDANCE ANALYSIS AND DISCUSSION

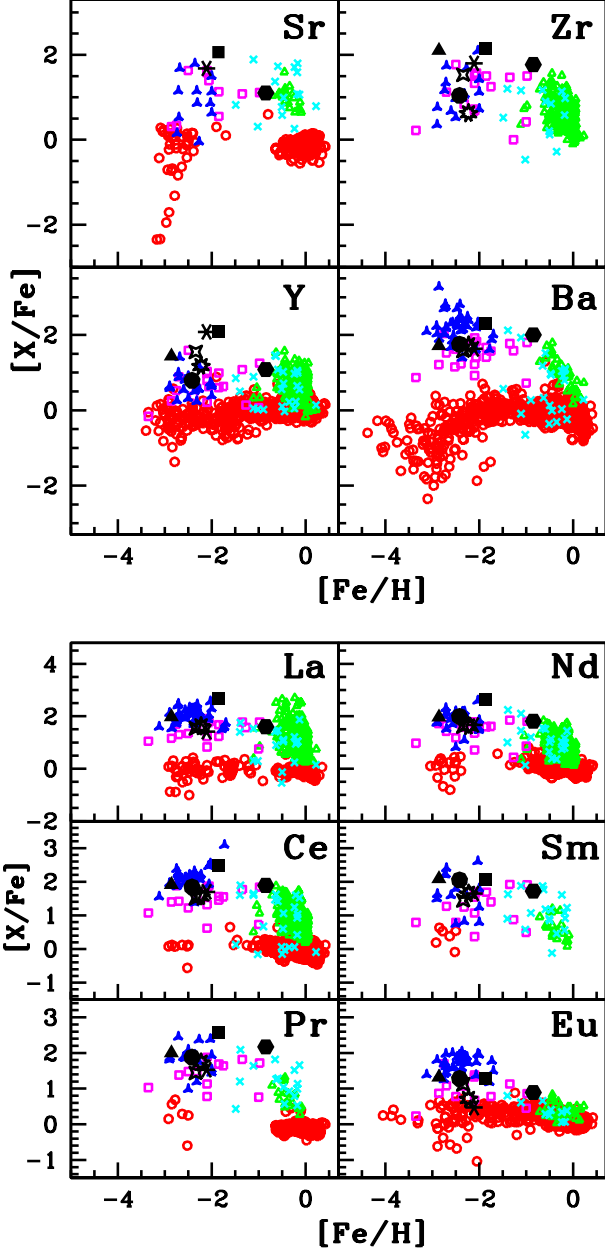
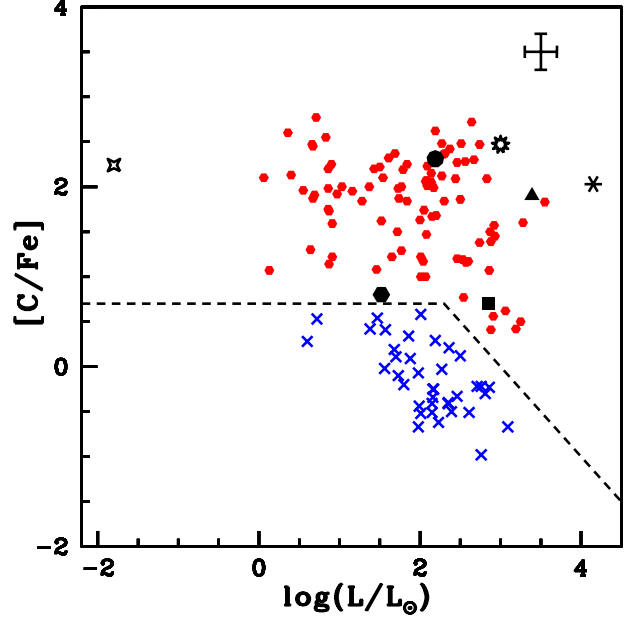
The detailed analysis of the abundance profiles of the program stars and their interpretation are discussed here.

### 8.1. CNO abundances

As mentioned in the previous section, the surface carbon abundance (as well as nitrogen and oxygen abundances) of a star is related to its evolutionary stage. When a star evolves into a red giant, the surface carbon abundance decreases due to the internal mixing that brings the CNO processed material from the stellar interiors to the surface, known as First Dredge-Up (FDU). Some extra mixing processes in addition to the internal mixing is also found to operate in more evolved giants. Here the mixing between the surface and the hydrogen burning layer where C is converted to N through CNO cycle in the upper RGB stars tends to decrease the carbon abundance further (Charbonnel 1995). This has been observed in more evolved metal-poor field giants (Charbonnel et al. 1998; Gratton et al. 2000; Spite et al. 2005, 2006) and Globular and open cluster giants (Gilroy 1989; Grundahl et al. 2002; Shetrone 2003; Jacobson et al. 2005). This internal mixing pro-

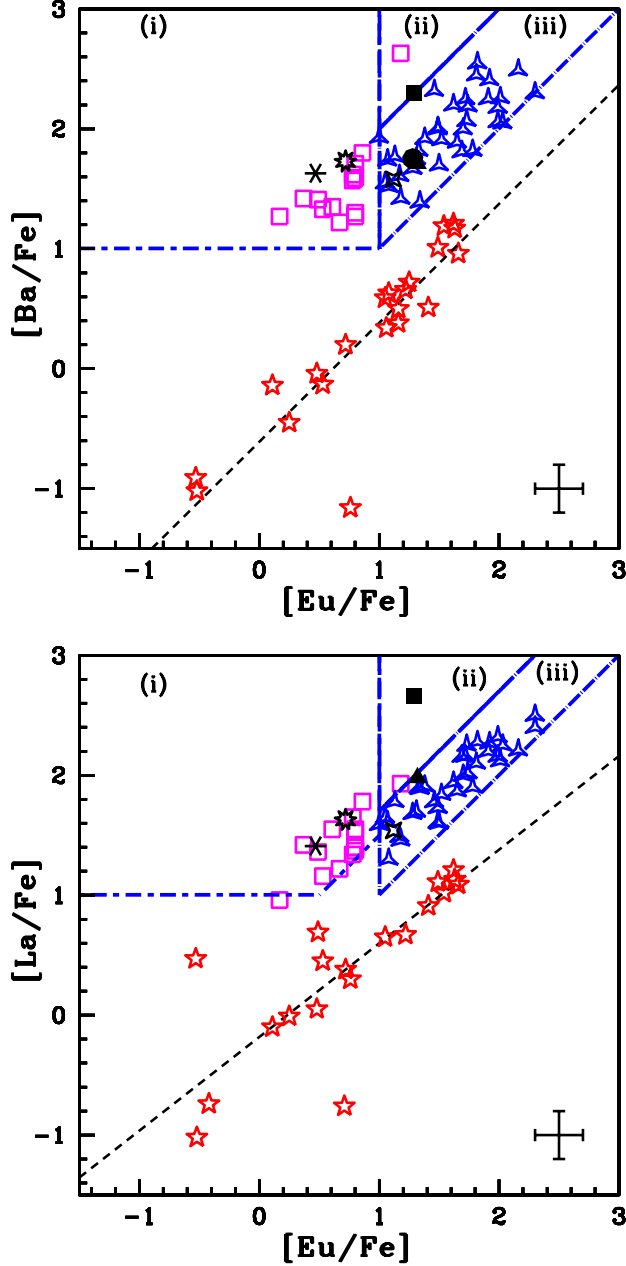
**Table 10.** The [Ba/Eu] and [La/Eu] ratios in the program stars

Star name	[Fe/H]	[C/Fe]	[Ba/Fe]	[Eu/Fe]	[Ba/Eu]	[La/Eu]
BD−19 132	−1.86	0.70	2.30	1.29	1.01	1.37
BD−19 290	−2.86	1.90	1.71	1.32	0.39	0.60
HE 1157−0518	−2.42	2.31	1.75	1.28	0.47	−
HE 1304−2111	−2.34	2.24	1.58	1.12	0.46	0.42
HE 1354−2257	−2.11	2.03	1.63	0.47	1.16	0.94
BD+19 3109	−2.23	2.47	1.73	0.72	1.01	0.85
HD 202851	−0.85	0.80	2.00	0.89	1.11	0.71


**Figure 9.** Observed [X/Fe] ratios of the heavy elements in the program stars with respect to metallicity [Fe/H]. Symbols have same meaning as in Figure 5

**Figure 10.** Observed [C/Fe] ratios as a function of  $\log(L/L_{\odot})$ . Red filled hexagons represent CEMP stars from literature (Aoki et al. 2007 and references therein, Goswami et al. 2016; Purandardas et al. 2019; Shejeelammal et al. 2021; Karinkuzhi et al. 2021; Goswami et al. 2021). Blue crosses represent carbon-normal metal-poor stars from literature (Aoki et al. 2005, 2007; Cayrel et al. 2004; Honda et al. 2004). BD−19 132 (filled square), BD−19 290 (filled triangle), HE 1157−0518 (filled circle), HE 1304−2111 (four-sided star), HE 1354−2257 (six-sided cross), BD+19 3109 (nine-sided star), and HD 202851 (filled hexagon). The threshold [C/Fe] is shown by the dashed line. A representative error bar is shown at the top right corner.

cesses result in an increase of nitrogen abundance at the expense of carbon and oxygen (CN and ON cycles).

Among our program stars, HE 1157−0518 and HD 202851 are found to be on the ascend of Red Giant Branch (RGB) (Figure 3,  $\log g = 2.52$  and  $2.20$  respectively), and all other stars are evolved giants ( $0.60 \leq \log g \leq 1.13$ ). The observed [C/Fe], [N/Fe], and [O/Fe] ratios of the program stars are shown in Figure 12. Carbon



**Figure 11.** Observed  $[\text{Ba}/\text{Fe}]$  (upper panel) and  $[\text{La}/\text{Fe}]$  (lower panel) as functions of observed  $[\text{Eu}/\text{Fe}]$  for CEMP and r stars. Magenta squares, blue starred triangles and red five-sided stars represent CEMP-s CEMP-r/s and r (including both CEMP-r and rI/rII stars) stars respectively from literature (Masseron et al. 2010; Shejeelammal et al. 2021; Karinkuzhi et al. 2021; Goswami et al. 2021). BD-19 132 (filled square), BD-19 290 (filled triangle), HE 1157-0518 (filled circle), HE 1304-2111 (four-sided star), HE 1354-2257 (six-sided cross), BD+19 3109 (nine-sided star), and HD 202851 (filled hexagon). Region (i) and (ii) are the CEMP-s and (iii) is CEMP-r/s star region as given by Goswami et al. (2021). The dashed line is the least-square fit to the observed abundances in r-stars. A representative error bar is shown at the bottom right corner of each panel.

abundance is available for all the program stars, nitrogen abundance for six stars and oxygen abundance for four stars. Five out of the seven program stars show  $[\text{C}/\text{Fe}]$ ,  $[\text{N}/\text{Fe}] > 1$  and one star show  $[\text{O}/\text{Fe}] > 1$ . While the five objects in our sample show similar  $[\text{C}/\text{Fe}]$  ratio, two objects BD-19 132 and HD 202851, show lowest (but similar)  $[\text{C}/\text{Fe}]$ . From the Figure 12, it is clear that, these two stars are enhanced in nitrogen and shows lowest  $[\text{O}/\text{Fe}]$ , may be an indication of CNO cycle and internal mixing. If that is the case, these stars are expected to show low  $[\text{C}/\text{N}]$  and high  $[\text{N}/\text{O}]$  ratio. According to Spite et al. (2005), the stars with  $[\text{C}/\text{N}] < -0.6$  are mixed stars and that with  $[\text{C}/\text{N}] > -0.6$  are unmixed stars. These two stars lie in the region of mixed stars and show higher  $[\text{N}/\text{O}]$  ratio (Figure 13). The Figure 12 combined with Figure 13 suggest that both CN and ON cycle might have operated in these two stars which altered the surface CNO abundances through mixing. If the nitrogen abundance is altered only due to the CN processing, then the  $[\text{C}+\text{N}/\text{Fe}]$  ratios of the mixed and unmixed stars will be similar, with lower  $^{12}\text{C}/^{13}\text{C}$  ratio for the mixed stars and if ON cycle also contributed to the N enhancement, such stars show  $[\text{C}+\text{N}]$  excess compared to the unmixed stars (Spite et al. 2005, 2006). But, both BD-19 132 and HD 202851 show lower  $[\text{C}+\text{N}/\text{Fe}]$  ratio compared to the other stars (Figure 14) and have relatively higher  $^{12}\text{C}/^{13}\text{C}$  ratio (18 and 42 respectively) (Table 4 and 5). This suggests that the nitrogen over abundance in these two stars may not have been resulted from an in-situ enhancement; it may be either the signature of a massive AGB companion with Hot-Bottom Burning (HBB) or the nitrogen enhanced primordial matter from which these stars have formed. We explore the possibility of HBB using different abundance ratios in the next few sections.

## 8.2. The $[\text{hs}/\text{ls}]$ ratio

The  $[\text{hs}/\text{ls}]$  ratio, heavy s-process elements to light s-process elements abundance ratio, is an indicator of s-process efficiency. At higher neutron exposures, second peak (hs) s-process elements are produced over the first peak (ls), resulting in high  $[\text{hs}/\text{ls}]$  ratio. As the neutron exposure increases with decreasing metallicity, the  $[\text{hs}/\text{ls}]$  ratio is anti-correlated with metallicity. Also the neutron source  $^{13}\text{C}(\alpha, n)^{16}\text{O}$  is found to be anti-correlated with metallicity (Clayton 1988; Wallerstein et al. 1997). Hence positive values for  $[\text{hs}/\text{ls}]$  ratio could be seen in low-mass, low metallicity AGB stars (Goriely & Mowlavi 2000; Busso et al. 2001). Whereas, in the case of massive AGB stars (5 - 8  $M_{\odot}$ ), where the neutron source is  $^{22}\text{Ne}(\alpha, n)^{25}\text{Mg}$ , negative values for this ratio is observed (Goriely & Siess 2005;

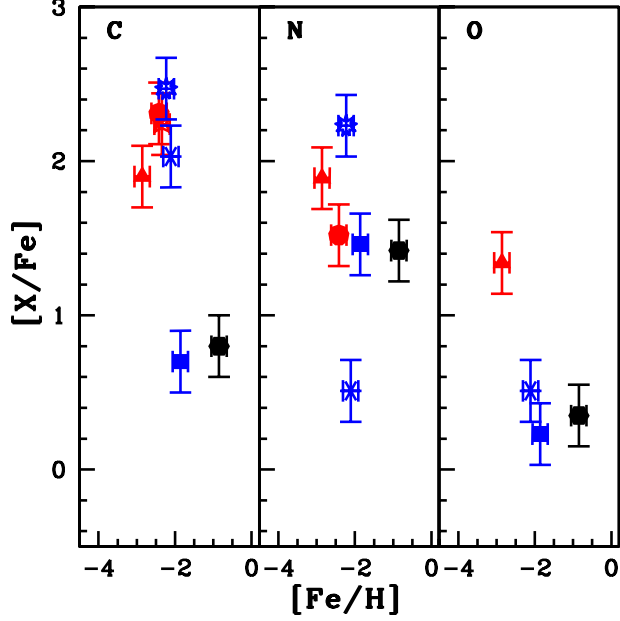


**Figure 12.** Observed  $[C/Fe]$ ,  $[N/Fe]$  and  $[O/Fe]$  as functions of observed  $[Fe/H]$  for the program stars. Red symbols are CEMP-r/s stars, blue symbols CEMP-s stars and black symbol CH star. BD–19 132 (filled square), BD–19 290 (filled triangle), HE 1157–0518 (filled circle), HE 1304–2111 (four-sided star), HE 1354–2257 (six-sided cross), BD+19 3109 (nine-sided star), and HD 202851 (filled hexagon).

Karakas 2010; Karakas et al. 2012; van Raai et al. 2012; Karakas & Lattanzio 2014).

The CEMP-r/s stars generally show higher  $[hs/ls]$  value compared to the CEMP-s stars (Abate et al. 2015; Hollek et al. 2015), however there is no clear distinction observed between the  $[hs/ls]$  ratios of the CEMP-r/s and CEMP-s stars. Analysis of Goswami et al. (2021) have shown that CEMP-s stars and CEMP-r/s stars peak at  $[hs/ls]$  values  $\sim 0.65 \pm 0.35$  and  $1.06 \pm 0.32$  respectively with an overlap between them in the range  $0 < [hs/ls] < 1.5$ . Karinkuzhi et al. (2021) also noted in their sample of CEMP stars the overlap of  $[hs/ls]$  ratio between CEMP-s and CEMP-r/s stars. The  $[hs/ls]$  ratio observed in our program stars are below 1.50 (Table 6), and we could not see any distinction between these two classes of stars in terms of  $[hs/ls]$  ratio (Figure 15). All the three CEMP-r/s stars in our sample show positive values of  $[hs/ls]$  and they are more metal-poor than the CEMP-s stars (right panel, Figure 15), as also noted by Karinkuzhi et al. (2021). All the stars except HE 1354–2257 show positive  $[hs/ls]$  ratio indicating a low-mass AGB companion. The star HE 1354–2257 has  $[hs/ls] \sim -0.24$ , indicating a clear over production of ls elements over hs elements, a trend observed in massive AGB stars. There are a few CEMP-s stars in literature

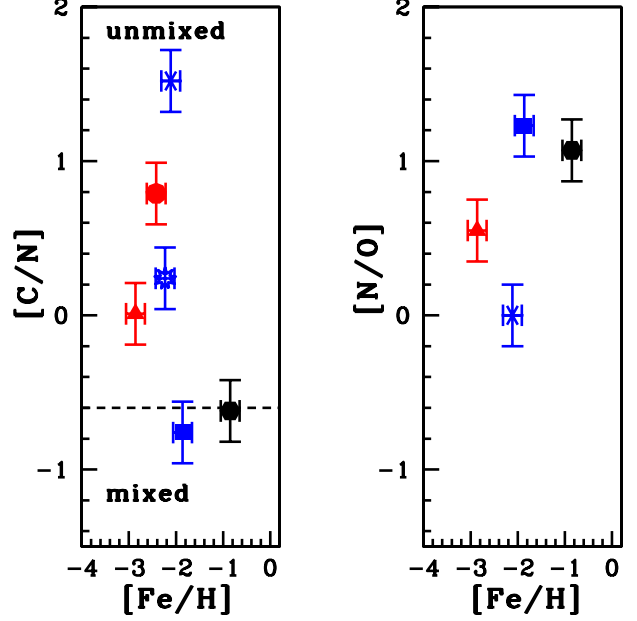


**Figure 13.** Observed  $[C/N]$  (left panel) and  $[N/O]$  (right panel) as functions of observed  $[Fe/H]$  for the program stars. BD–19 132 (filled square), BD–19 290 (filled triangle), HE 1157–0518 (filled circle), HE 1304–2111 (four-sided star), HE 1354–2257 (six-sided cross), BD+19 3109 (nine-sided star), and HD 202851 (filled hexagon).

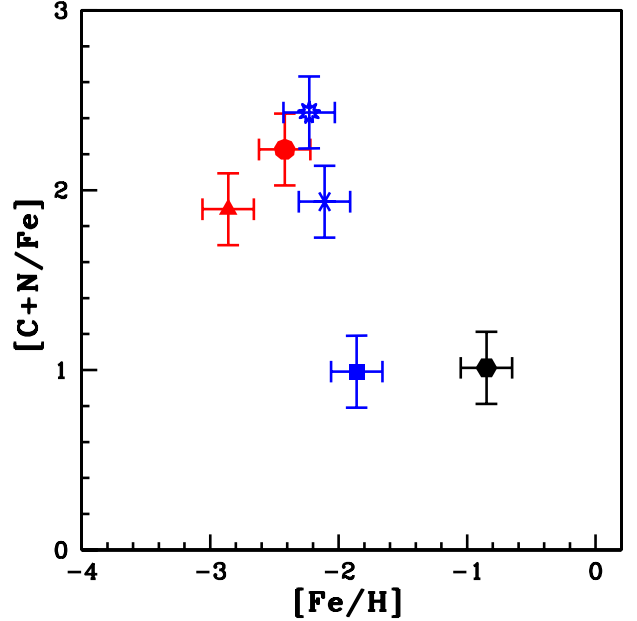


**Figure 14.** Observed  $[C+N/Fe]$  ratio as functions of observed  $[Fe/H]$  for the program stars. BD–19 132 (filled square), BD–19 290 (filled triangle), HE 1157–0518 (filled circle), HE 1304–2111 (four-sided star), HE 1354–2257 (six-sided cross), BD+19 3109 (nine-sided star), and HD 202851 (filled hexagon).

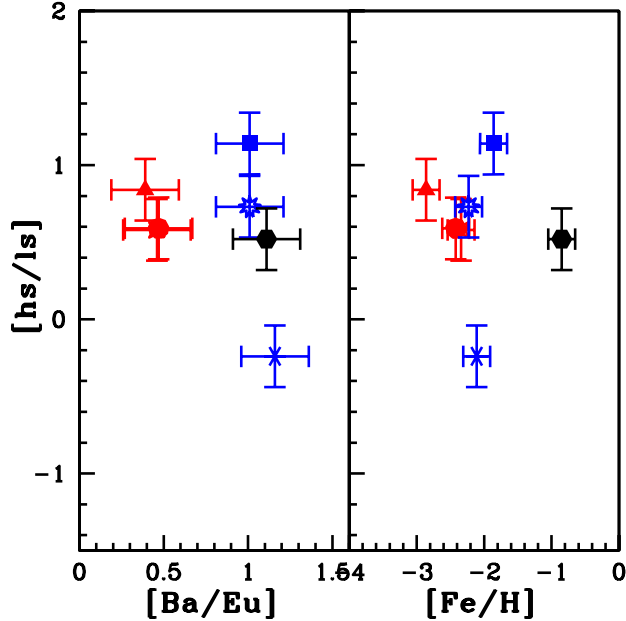


**Figure 15.** The  $[hs/ls]$  ratio as a function of  $[Ba/Eu]$  (left panel) and  $[Fe/H]$  (right panel) for the program stars. Red symbols are CEMP-r/s stars, blue symbols CEMP-s stars and black symbol CH star. BD-19 132 (filled square), BD-19 290 (filled triangle), HE 1157-0518 (filled circle), HE 1304-2111 (four-sided star), HE 1354-2257 (six-sided cross), BD+19 3109 (nine-sided star), and HD 202851 (filled hexagon).

that show negative values for  $[hs/ls]$  ratio; for instance, Hansen et al. (2019) present a star HE 2158-5134 that shows  $[hs/ls] \sim -0.15$  and Aoki et al. (2002) noted a value  $\sim -0.36$  for the object CS 22942-019. Analysis of Bisterzo et al. (2011) have shown that the abundance pattern in CS 22942-019 could be reproduced with 1.5  $M_{\odot}$  AGB model.

### 8.3. Na, Mg, and heavy elements

Three out of the six program stars for which we could estimate the Na abundance are enhanced in Na with  $[Na/Fe] > 1$  and HE 1304-2111 being the most enhanced with  $[Na/Fe] \sim 2.83$ . Similar value of sodium enhancement is observed in a CEMP-r/s star CS 29528-028 which shows  $[Na/Fe] \sim 2.68$  (Aoki et al. 2007). They considered this star to be an extreme case of Ba-enhanced CEMP star. The Na enhancement through Ne-Na cycle is expected in massive AGB stars where HBB operates. HBB also results in an increased surface abundance of N through the CN cycle (Sugimoto 1971; Lattanzio et al. 1996; Goriely & Siess 2005; Karakas & Lattanzio 2003, 2014; Ventura & D’Antona 2005). Since the HBB is responsible for the over-production of N and Na in massive stars, they should be correlated if the abundance

peculiarity is the result of massive-AGB stars nucleosynthesis. But we could not see any such trend in our sample of program stars (Figure 16, top panel, left column). The diffusive mixing and H-burning in these massive-AGB stars can reduce the s-process efficiency and it should be anti-correlated with the products of HBB (Goriely & Siess 2005). However, we have not noticed any such behaviour among our program stars (Figure 16, top panel, right column). Enhanced Mg is also expected in them, resulting from the  $\alpha$ -capture reaction of  $^{22}\text{Ne}$ , and hence, similar behaviour as seen in the case of Na, is also expected for Mg. A slight trend could be noted in  $[Mg/Fe]$  v/s  $[N/Fe]$  plot (Figure 16, bottom panel, left column), however the scatter in the  $[Mg/Fe]$  v/s  $[s/Fe]$  plot (Figure 16, bottom panel, right column) suggests, that the trend may not be real. So these facts together with the positive  $[hs/ls]$  ratio observed in three Na enhanced stars as discussed in the previous section, rules out the possibility of the HBB and massive AGB star pollution.

The object HE 1354-2257 with negative  $[hs/ls]$ , as discussed in section 8.2, does not show any N, Na, and Mg enhancement. So this discards the possibility of a massive AGB star companion. Similarly, for the objects BD-19 132 and HD 202851 discussed in section 8.1, we rule out the possibility of massive AGB star companions.

The AGB models of Bisterzo et al. (2010) predict higher Na abundances at lower metallicities. They have studied the nucleosynthesis in low-mass AGB stars ( $M_{\text{AGB}}^{\text{ini}} \sim 1.3 - 2 M_{\odot}$ ) of metallicities  $-3.6 \leq [Fe/H] \leq -1$  for different  $^{13}\text{C}$  pocket efficiencies. The major neutron source here is  $^{13}\text{C}(\alpha, n)^{16}\text{O}$  reaction during the inter-pulse phase. The source  $^{22}\text{Ne}(\alpha, n)^{25}\text{Mg}$  is also considered to be partially activated during the TP. This models include the production of primary  $^{23}\text{Na}$  produced through a chain of TP/TDU/IP events from the  $^{12}\text{C}$ . The primary  $^{12}\text{C}$  produced by the  $3\alpha$ -reaction are brought to the surface from the inter-shell region by the TDU. During the following inter-pulse, the  $^{12}\text{C}$  is transformed into  $^{14}\text{N}$  through CNO cycle by the H-burning shell and accumulated in the top layers of the inter-shell-region. This  $^{14}\text{N}$  is converted to  $^{22}\text{Ne}$  during the early phase of next thermal instability via  $^{14}\text{N}(\alpha, \gamma)^{18}\text{F}(\beta^+ \nu)^{18}\text{O}(\alpha, \gamma)^{22}\text{Ne}$  (Mowlavi 1999; Gallino et al. 2006). This  $^{22}\text{Ne}$  results in the primary production of the  $^{23}\text{Na}$  via the n-capture reaction  $^{22}\text{Ne}(n, \gamma)^{23}\text{Ne}(\beta^- \nu)^{23}\text{Na}$  that are significant at low-metallicities (Gallino et al. 2006; Bisterzo et al. 2011). The amount of the primary Na produced increases with decreasing metallicity and/or increasing  $M_{\text{AGB}}^{\text{ini}}$  (Figure 15 of Bisterzo et al. 2010). Bisterzo et al. (2011) performed a comparison of abun-

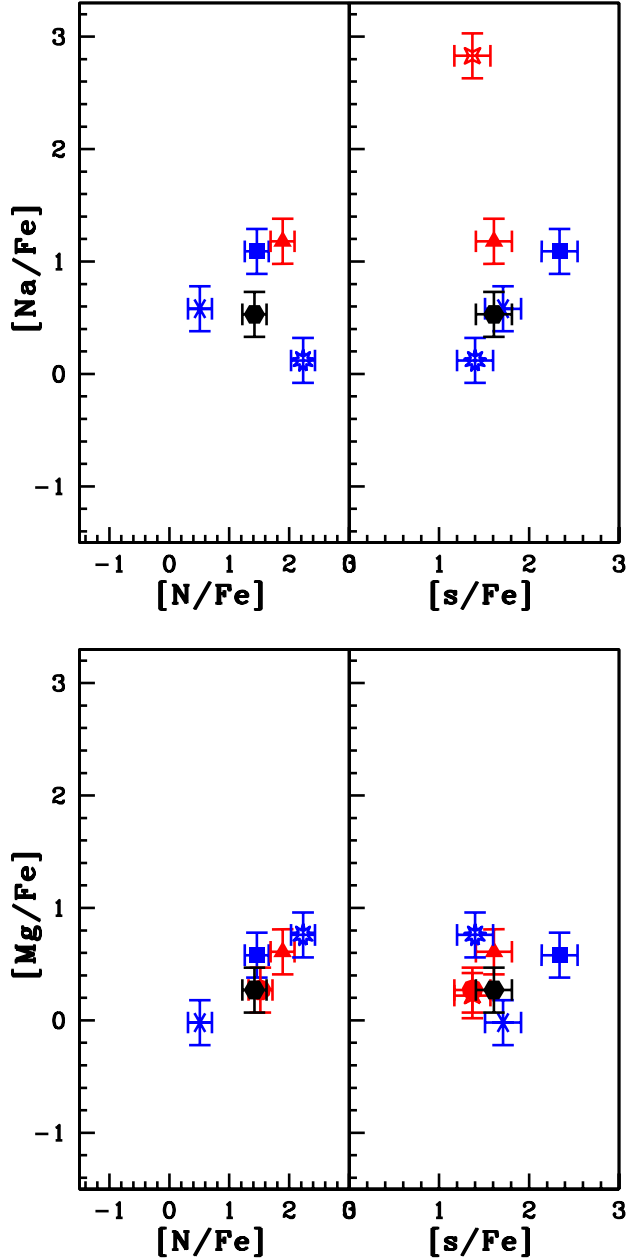


**Figure 16.** The observed  $[\text{Na}/\text{Fe}]$  (upper panel) and  $[\text{Mg}/\text{Fe}]$  (lower panel) ratios as a function of  $[\text{N}/\text{Fe}]$  and  $[\text{s}/\text{Fe}]$  for the program stars. Red symbols are CEMP-r/s stars, blue symbols CEMP-s stars and black symbol CH star. BD-19 132 (filled square), BD-19 290 (filled triangle), HE 1157-0518 (filled circle), HE 1304-2111 (four-sided star), HE 1354-2257 (six-sided cross), BD+19 3109 (nine-sided star), and HD 202851 (filled hexagon).

dance patterns of a sample of 100 CEMP-s stars collected from literature with the AGB nucleosynthesis models of [Bisterzo et al. \(2010\)](#). Among this sample, nine stars show  $[\text{Na}/\text{Fe}] \geq 1$  with two stars showing  $[\text{Na}/\text{Fe}] \geq 2$ , CS 29528-028 ( $[\text{Fe}/\text{H}] \sim -2.86$ ,

$[\text{Na}/\text{Fe}] \sim 2.68$  [Aoki et al. 2007](#)) and SDSS 1707+58 ( $[\text{Fe}/\text{H}] \sim -2.52$ ,  $[\text{Na}/\text{Fe}] \sim 2.71$  [Aoki et al. 2008](#)). Their analysis have shown that, the AGB models with  $M_{\text{AGB}}^{\text{ini}} \sim 1.5 M_{\odot}$  could reproduce the Na abundances observed in them, but not the entire observed abundances.

#### 8.4. The $[\text{Rb}/\text{Zr}]$ ratio

The  $[\text{Rb}/\text{Zr}]$  ratio is an important indicator of neutron density at the s-process site and the mass of the companion AGB stars. In massive AGB stars ( $M \geq 4 M_{\odot}$ ), where the neutron source is  $^{22}\text{Ne}(\alpha, n)^{25}\text{Mg}$  reaction ( $n \sim 10^8$  neutrons/cm<sup>3</sup>), a higher Rb abundance and hence a positive value for  $[\text{Rb}/\text{Zr}]$  ratio are predicted ([Abia et al. 2001](#); [van Raaij et al. 2012](#)), whereas, in the low-mass AGB stars ( $M \leq 3 M_{\odot}$ ) where  $^{13}\text{C}(\alpha, n)^{16}\text{O}$  is the major neutron source ( $n \sim 10^{13}$  neutrons/cm<sup>3</sup>), a negative  $[\text{Rb}/\text{Zr}]$  ratio is predicted ([Karakas et al. 2012](#)). This has been supported by the observations of low- and intermediate-mass AGB stars of the Galaxy and Magellanic Clouds. ([Plez et al. 1993](#); [Lambert et al. 1995](#); [Abia et al. 2001](#); [García-Hernández et al. 2006, 2007, 2009](#)). We have presented a detailed discussion on this ratio in [Shejeelammal et al. \(2020\)](#). The estimated values of the neutron density dependent  $[\text{Rb}/\text{Zr}]$  ratio for our program stars are given in Table 6. All the four stars where we could estimate this ratio show a negative value, indicating a low-mass AGB companion. The observed range of  $[\text{Rb}/\text{Fe}]$  and  $[\text{Zr}/\text{Fe}]$  in our program stars along with that in the massive AGB stars is shown in Figure 17 for a comparison.

#### 8.5. Binary status of the program stars

The analysis of [Spite et al. \(2013\)](#) for a sample of dwarf and main-sequence turn-off CEMP stars ( $\sim 50$ ) from literature ( $[\text{Fe}/\text{H}] < -1.80$ ) have shown that the CEMP stars show bimodality in the absolute carbon abundance, that is, they show two distinct absolute carbon abundance  $A(\text{C})$ , values. The stars with  $[\text{Fe}/\text{H}] \geq -3.4$  (CEMP-s and CEMP-r/s) populate the high carbon region at  $A(\text{C}) \sim 8.25$  and the stars with  $[\text{Fe}/\text{H}] < -3.4$  (CEMP-no) populate the low carbon region at  $A(\text{C}) \sim 6.80$ . This analysis did not consider any giants so as to avoid any carbon dilution resulting from any mixing processes. Later, [Bonifacio et al. \(2015\)](#) confirmed the bimodality of CEMP stars from an extended sample of CEMP stars that included dwarfs and main-sequence turn-off stars along with a few subgiants and lower RGB giants. In both the studies, they noted a clear separation between the two carbon bands. Their interpretation of this bimodality is that, the carbon in the stars of these two carbon bands have differ-

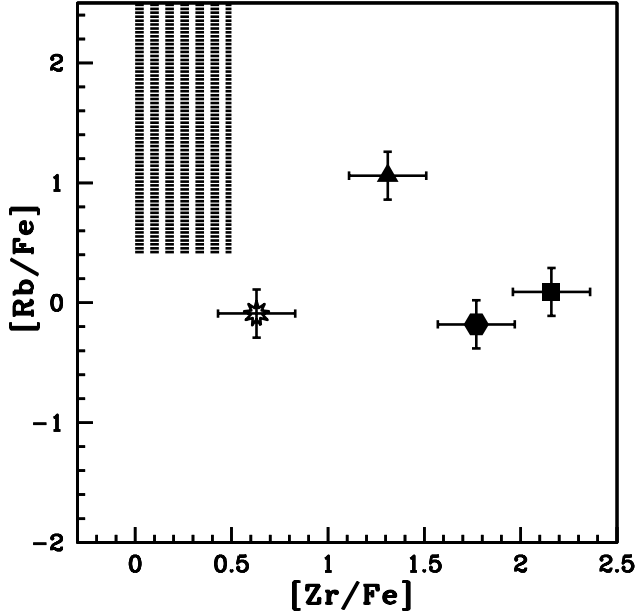


**Figure 17.** The observed  $[Rb/Fe]$  and  $[Zr/Fe]$  in the program stars. BD-19 132 (filled square), BD-19 290 (filled triangle), BD+19 3109 (nine-sided star), and HD 202851 (filled hexagon). The observed ranges of  $[Rb/Fe]$  and  $[Zr/Fe]$  in intermediate-mass AGB stars of the Galaxy and the Magellanic Clouds (van Raai et al. 2012) are shown as shaded region.

ent astrophysical origin. The carbon in the high carbon band stars are of extrinsic origin - resulting from the mass transfer from a low-mass AGB companion and that in the low carbon band stars owe to an intrinsic origin - C-enriched ISM from which they were formed despite a few of them are binaries as noted by Starkenburg et al. (2014) (Bonifacio et al. 2015). Subsequently, Hansen et al. (2015b) also noted the bimodal carbon distribution for their sample of ( $\sim 64$ ) CEMP stars. However they found a smooth transition between the two carbon bands, in contrast to the well separated bands reported by Spite et al. (2013) and Bonifacio et al. (2015), with three CEMP-no stars occupying the high carbon band. This observation pointed to the importance of the knowledge of the binary status of the CEMP stars in order to better constrain the accurate origin of the observed abundances in the CEMP sub-classes.

In an attempt to address this question, Yoon et al. (2016) have compiled an extensive set of 305 CEMP stars from literature with  $[Fe/H] < -1$  and  $[C/Fe] \geq 0.70$ . The sample comprised of 147 CEMP-s and CEMP-r/s stars (together they denoted as CEMP-s stars) and 127 CEMP-no stars, out of which, the binary status of 35 CEMP-s and 22 CEMP-no stars are known. They also

noted the carbon bimodality, but at  $A(C)$  values lower than that noted by Spite et al. (2013); the low- and high- carbon bands peaking at  $A(C) \sim 6.28$  and  $7.96$  respectively. Based on the behaviour of  $A(C)$  with respect to  $[Fe/H]$ , these stars were grouped into three groups; CEMP-s stars being the members of Group I and CEMP-no stars being Group II and III objects. Their analysis have confirmed the interpretation put forward by Spite et al. (2013) and Bonifacio et al. (2015) for the origin of carbon. Also they presented  $A(C) - [Fe/H]$  diagram as a powerful tool to distinguish between the CEMP-no and CEMP-s/(r/s) sub-classes. According to this study, the absolute carbon abundance  $A(C) \sim 7.1$  separates majority of binary stars, which lie above this carbon abundance, from single stars despite of a few outliers. Also, stars with  $A(C) \leq 7.1$  are classified as CEMP-no stars and that with  $A(C) > 7.1$  are classified as CEMP-s/(r/s) stars.

We have used  $A(C) - [Fe/H]$  plot to understand the binary nature of our program stars. Before using this diagram for this purpose, the carbon abundance should be corrected to account for any internal mixing. Placco et al. (2014) have calculated the corrections to the carbon abundance for  $0.0 \leq \log g \leq 5.0$ ,  $-5.5 \leq [Fe/H] \leq 0.00$ , and  $-1.0 \leq [C/Fe] \leq 3.0$ . We have obtained the corrections to the estimated carbon abundances of our program stars using the public online tool (<http://vplacco.pythonanywhere.com/>) developed by Placco et al. (2014). The necessary corrections have been applied to our estimates of carbon abundance and then used in the Figure 18. The star HD 202851 lie among the CH stars and other program stars lie among the CEMP-s/(r/s) stars, with all the stars lying in the high carbon band. It is also noted that all our program stars lie in the region of binary stars that bear the signatures of binary mass transfer from the low-mass AGB companions according to Bonifacio et al. (2015). As discussed in section 3, the stars BD+19 3109 and HD 202851 are confirmed binaries. The difference in the estimated radial velocities of the stars BD-19 132, BD-19 290, and HE 1304-2111 from the literature values discussed in section 3 along with their position in the  $A(C) - [Fe/H]$  diagram suggest that these stars are possible binaries.

### 8.6. Parametric model based analysis

CEMP-s stars are known to be the products of binary mass transfer from low-mass AGB companion which now evolved into an invisible White Dwarf. However, a number of scenarios have been proposed till date to explain the origin of CEMP-r/s stars, enriched in both s- and r-process elements. Detailed discussions on several scenar-

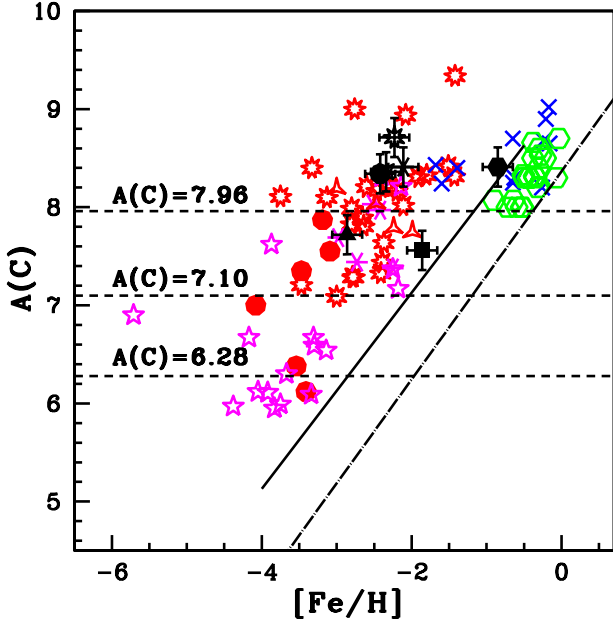


**Figure 18.** Distribution of  $A(C)$  as a function of  $[Fe/H]$  for known/likely binary and single stars. Red nine-sided stars, magenta six-sided crosses, red starred triangles, red filled circles and magenta five-sided stars represent binary CEMP-s, single CEMP-s, binary CEMP-r/s, binary CEMP-no, and single CEMP-no stars respectively from literature (Yoon et al. 2016). All the red symbols corresponds to the binary CEMP stars and magenta symbols to single CEMP stars. Blue crosses represent the binary CH stars from literature (Purandardas et al. 2019; Karinkuzhi & Goswami 2014, 2015; Luck 2017). Binary Ba stars from literature (Shejeelammal et al. 2020; Karinkuzhi et al. 2018) are represented by green open hexagons. BD-19 132 (filled square), BD-19 290 (filled triangle), HE 1157-0518 (filled circle), HE 1304-2111 (four-sided star), HE 1354-2257 (six-sided cross), BD+19 3109 (nine-sided star) and HD 202851 (filled hexagon). The binary and single stars are separated by the dashed line at  $A(C) = 7.10$ . The solid line corresponds to  $[C/Fe] = 0.70$  and long-dash dot line to  $[C/Fe] = 0$ .

ios are available in many places (i.e., Jonsell et al. 2006; Goswami et al. 2021 and references therein). Most of these scenarios suggested an independent origin for the s- and r- process enrichment in CEMP-r/s stars. Analysis of Abate et al. (2016) have shown that these proposed scenarios have failed to reproduce the observed frequency ( $\sim 54\%$ ) and higher  $[hs/ls]$  ratio of the CEMP-r/s stars. From the analysis of a sample of CEMP stars ( $\sim 18$ ), Allen et al. (2012) argued that CEMP-r/s stars have the same astrophysical origin as CEMP-s stars.

The overlap of  $[hs/ls]$  ratio between the CEMP-s and CEMP-r/s stars indicates that the origin of both the groups of stars owe a common astrophysical site and process but under different conditions. The higher

$[hs/ls]$  ratio, more precisely the higher  $[hs/Fe]$  ratio of the CEMP-r/s stars compared to the CEMP-s stars indicate a high neutron density process for their formation than the classical s-process. The tight correlation between the observed  $[Eu/Fe]$  and  $[hs/Fe]$  ratios in CEMP-r/s stars (Figure 13(c) of Goswami et al. 2021) also points towards a single stellar site where both the s- and r- process elements could be produced simultaneously. The low-metallicity and high  $[hs/Fe]$  ratio suggest the extreme conditions of low-mass and low-metallicity s-process. The intermediate neutron-capture process, i-process, originally proposed by Cowan & Rose (1977), has been explored recently by several authors to explain the CEMP-r/s phenomena (Dardelet et al. 2014; Hampel et al. 2016, 2019; Hansen et al. 2016b). A higher neutron densities than that required for the classical s-process, of the order of  $10^{15} - 10^{17} \text{ cm}^{-3}$ , intermediate between the s- and r-process neutron densities, could be achieved as a result of proton Ingestion Episodes (PIEs; mixing of hydrogen rich material to the intershell region) in evolved red giants (Cowan & Rose 1977). There are several proposed sites for the PIEs that include low-metallicity low-mass AGB stars ( $z \leq 10^{-4}$ ,  $M \leq 2M_{\odot}$ ) (Fujimoto et al. 2000; Campbell & Lattanzio 2008; Lau et al. 2009; Cristallo et al. 2009; Campbell et al. 2010; Stancliffe et al. 2011; Cruz et al. 2013) etc., massive super-AGB stars (Doherty et al. 2015; Jones et al. 2016), post-AGB stars (Herwig et al. 2011, 2014; Bertolli et al. 2013; Woodward et al. 2015), Rapidly Accreting White Dwarfs (RAWD; Denissenkov et al. 2019) etc. A discussion on the several proposed sites of PIEs is given in Goswami et al. (2021).

Hampel et al. (2016) successfully used the simulations based on the i-process occurring in the low-mass low-metallicity ( $1 M_{\odot}$ ,  $z \sim 10^{-4}$ ) AGB stars to reproduce the observed abundance pattern of 20 CEMP-r/s stars. Later, this method has been extended successfully to a sample of seven low-Pb post-AGB stars in the magellanic cloud (Hampel et al. 2019). We have used the i-process model yields  $[X/Fe]$ , from Hampel et al. (2016) and compared with the observed  $[X/Fe]$  of our program stars for the neutron densities ranging from  $10^9$  to  $10^{15} \text{ cm}^{-3}$ . The observed abundances are fitted with the parametric model function;

$$X = X_i \cdot (1-d) + X_{\odot} \cdot d$$

where  $X$  represents the final abundance,  $X_i$  the i-process abundance,  $d$  is the dilution factor and  $X_{\odot}$  is the solar-scaled abundance. Here  $d$  is a free parameter that can be varied to find the best fit between the model and the

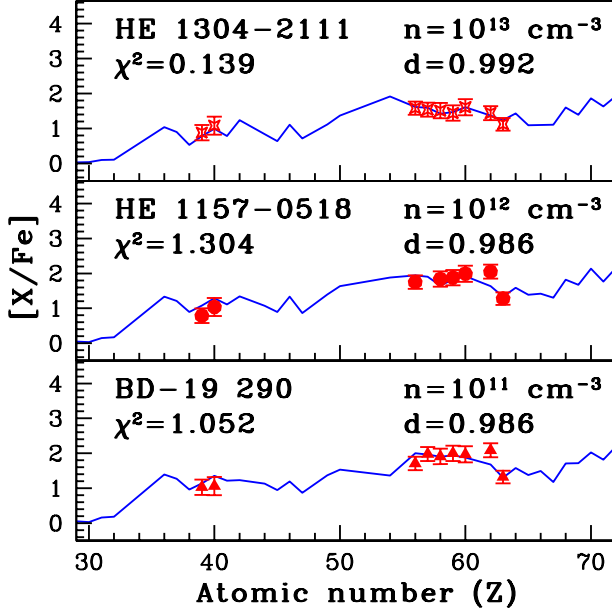


**Figure 19.** Solid curves represent the best fit for the parametric model function. The points with error bars indicate the observed abundances

observational data for each constant neutron density. The best fit model is found using  $\chi^2_{\min}$  method, where  $\chi^2$  is defined as;

$$\chi^2 = \sum_Z \frac{([X_Z/\text{Fe}]_{\text{obs}} - [X_Z/\text{Fe}]_{\text{mod}})^2}{\sigma_{Z,\text{obs}}^2}$$

where  $[X_Z/\text{Fe}]_{\text{obs}}$ ,  $[X_Z/\text{Fe}]_{\text{mod}}$  the observed and model abundances of the element with atomic number  $Z$  and  $\sigma_{Z,\text{obs}}^2$ , the observational uncertainty on  $[X_Z/\text{Fe}]_{\text{obs}}$ . The best fit model is selected in such a way that it shows least deviation from the observation, that is by minimizing the  $\chi^2$ . The best fits obtained for the CEMP-r/s stars are shown in Figure 19. The neutron density responsible for the observed abundances in the stars BD-19 290, HE 1157-0518, and HE 1304-2111 are found to be  $n \sim 10^{11}$ ,  $10^{12}$ , and  $10^{13}$  respectively.

We have also conducted a parametric model based analysis for the CEMP-s and CH stars in our sample to find the mass of their AGB companion stars. The observed abundances in these stars are compared with the predicted abundances for AGB stars from FRUITY (FRANEC Repository of Updated Isotopic Tables & Yields) models (Cristallo et al. 2009, 2011, 2015). The best fitting mass of the companion AGB is derived by fitting the observed abundance with the parametric model function of Husti et al. (2009) by minimizing the  $\chi^2$  value. The detailed procedure is given in Shejeelammal et al. (2020). The best fits obtained for these stars are given in Figure 20. The object

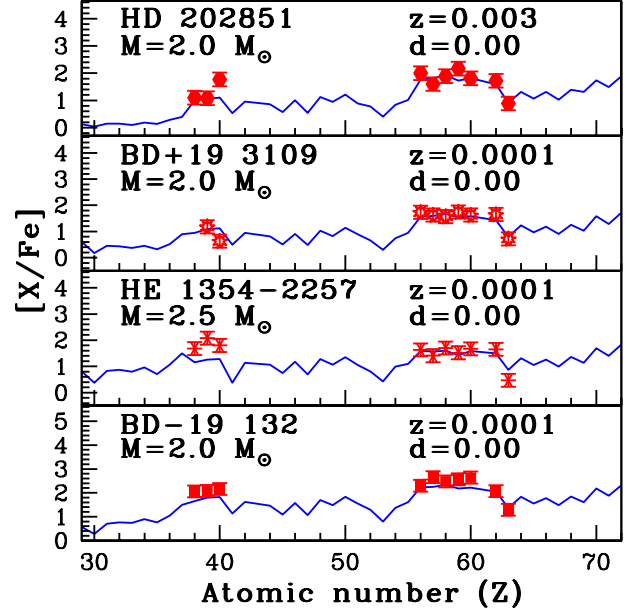


**Figure 20.** Solid curves represent the best fit for the parametric model function. The points with error bars indicate the observed abundances

HE 1354-2257 is found to have a companion of mass  $M \sim 2.5 M_{\odot}$  while the other three objects, BD-19 132, BD+19 3109, and HD 202851 have companions with mass  $M \sim 2.0 M_{\odot}$ .

### 8.7. Discussion on individual stars

In this section we provide a discussion on the individual stars summarizing the results of the above analyses.

**BD-19 132, BD-19 290, BD+19 3109:** These object are listed in the CH star catalogue of Bartkevicius (1996). We present, the first time abundance analysis results for these objects. Our analysis have shown that BD-19 132 and BD+19 3109 are CEMP-s stars and BD-19 290 is a CEMP-r/s star. BD+19 3109 is a confirmed binary with a period of  $2129 \pm 13$  days (Sperauskas et al. 2016). We found that BD-19 290 and BD+19 3109 are high radial velocity objects ( $|V_r| > 100 \text{ km s}^{-1}$ ) and BD-19 132 is a low radial velocity ( $|V_r| < 17 \text{ km s}^{-1}$ ) object. Yamashita (1975) classified BD+19 3109 as CH like star. Kinematic analysis have shown that BD-19 132 belongs to the Galactic thin disk and BD-19 290 and BD+19 3109 belong to the Galactic halo populations. From the neutron density dependent  $[\text{Rb}/\text{Zr}]$  ratio, these objects are found to have low-mass AGB companions.

**HE 1157-0518:** This object is a VMP star with  $[\text{Fe}/\text{H}] \sim -2.42$ . This object is listed among the faint

high latitude carbon stars identified from the HES survey (Christlieb et al. 2001a). Aoki et al. (2007) could not determine the Eu abundance for this object, however, they have classified it as a CEMP-s star. Our analysis shows this star to be a CEMP-r/s star. Our estimates of atmospheric parameters are in agreement with that of Aoki et al. (2007) except for  $\log g$  which is 0.5 dex lower than our estimate. The abundances of C, N, Mg, Ca, Ti, and Cr also match well within the error limits. However, our estimate  $[\text{Ba}/\text{Fe}] \sim 1.75$  is  $\sim 0.40$  dex lower than their estimate. This object is found to be a member of Galactic halo with a probability of 100%. It is a high spatial velocity and high radial velocity object.

**HE 1304–2111, HE 1354–2257:** Both these objects are found to be very metal poor stars with  $[\text{Fe}/\text{H}] \sim -2.34$  and  $-2.11$  respectively. Ours is the first time abundance analysis for these objects. HE 1304–2111 is found to be a CEMP-r/s star whereas the latter is a CEMP-s star. While HE 1304–2111 is a disk object, HE 1354–2257 is found to belong to the Galactic halo population.

**HD 202851:** This object is listed in the CH star catalogue of Bartkevicius (1996). Our analysis shows this star to be a CH giant with  $[\text{Fe}/\text{H}] \sim -0.85$ . Sperauskas et al. (2016) confirmed this object to be a binary with a period of  $1295 \pm 6$  days from radial velocity studies. HD 202851 is found to be a low velocity object that belongs to the Galactic thin disk with 72% probability. The estimated atmospheric parameters of this star by Sperauskas et al. (2016) ( $T_{\text{eff}}$ ,  $\log g$ ,  $\zeta$ ,  $[\text{Fe}/\text{H}]$ ) (4800 K, 2.1, 1.5,  $-0.70$ ) are in close agreement with our estimates, (4900 K, 2.2, 1.54,  $-0.85$ ). Arentsen et al. (2019b) determined the atmospheric parameters of this star from medium-resolution ( $(\lambda/\delta\lambda \sim 10,000)$ ) spectra obtained with X-shooter spectrograph (Vernet et al. 2011) of Very Large Telescope (VLT). Their estimates for  $T_{\text{eff}}$ ,  $\log g$ , and  $[\text{Fe}/\text{H}]$  are 4733 K, 1.6, and  $-0.88$ . The negative value obtained for the  $[\text{Rb}/\text{Zr}]$  ratio in this star confirms low-mass AGB companion for HD 202851.

## 9. CONCLUSIONS

Detailed spectroscopic analyses of seven potential CH/CEMP stars are carried out based on the high-quality, high-resolution spectra obtained with HCT/HESP and SUBARU/HDS. We have estimated the abundances of twenty eight elements including both light and neutron-capture process elements and carbon isotopic ratio. We present the first time abun-

dance analysis for the objects BD–19 132, BD–19 290, HE 1304–2111, HE 1354–2257, and BD+19 3109.

The objects BD+19 3109 and HD 202851 are confirmed binaries. The difference in the estimated radial velocities of the stars BD–19 132, BD–19 290, and HE 1304–2111 from the Gaia values may be a robust indication that they are likely binaries. In the A(C) -  $[\text{Fe}/\text{H}]$  diagram, all the program stars fall in the region occupied by the binary stars. The kinematic analysis shows that the three low radial velocity objects in our sample BD–19 132, HE 1304–2111, and HD 202851, are members of Galactic disk population and the rest four high radial velocity objects belong to the Galactic halo population. From the position on the HR diagram, the objects BD–19 290, HE 1157–0518, and HD 202851 are found to be low mass objects ( $\sim 1M_{\odot}$ ).

All the objects in our sample are bona-fide CEMP stars, except HD 202851 which is found to be a CH star. Three objects BD–19 132, HE 1354–2257, and BD+19 3109 are CEMP-s stars, whereas BD–19 290, HE 1157–0518, and HE 1304–2111 are found to be CEMP-r/s stars. Our analysis based on different abundance ratios and abundance profiles confirmed low-mass AGB companions of the program stars. The i-process models could successfully reproduce the observed abundances of the CEMP-r/s stars. The parametric model based analysis performed for the CEMP-s and CH stars confirms former low-mass AGB companions with mass  $M \leq 2.5 M_{\odot}$ .

## 10. ACKNOWLEDGMENT

We thank the staff at IAO and at the remote control station at CREST, Hosakotte for assisting during the observations. Funding from the DST SERB project No. EMR/2016/005283 is gratefully acknowledged. We are thankful to Partha Pratim Goswami for generating the model fits used in Figure 19. This work made use of the SIMBAD astronomical database, operated at CDS, Strasbourg, France, and the NASA ADS, USA. This work has made use of data from the European Space Agency (ESA) mission Gaia (<https://www.cosmos.esa.int/gaia>), processed by the Gaia Data Processing and Analysis Consortium (DPAC, <https://www.cosmos.esa.int/web/gaia/dpac/consortium>). This research is based [in part] on data collected at Subaru Telescope, which is operated by the National Astronomical Observatory of Japan. We are honored and grateful for the opportunity of observing the Universe from Maunakea, which has the cultural, historical and natural significance in Hawaii.

**Data Availability**

The data underlying this article will be shared on reasonable request to the authors.

## REFERENCES

- Abate, C., Pols, O. R., Izzard, R. G., & Karakas, A. I. 2015, *A&A*, 581, A22
- Abate, C., Stancliffe, R. J., & Liu, Z.-W. 2016, *A&A*, 587, A50
- Abia, C., Busso, M., Gallino, R., et al. 2001, *ApJ*, 559, 1117
- Allen, D. M., & Barbuy, B. 2006, *A&A*, 454, 895
- Allen, D. M., Ryan, S. G., Rossi, S., Beers, T. C., & Tsangarides, S. A. 2012, *A&A*, 548, A34
- Alonso, A., Arribas, S., & Martínez-Roger, C. 1999, *A&AS*, 140, 261
- . 2001, *A&A*, 376, 1039
- Andrievsky, S. M., Spite, M., Korotin, S. A., et al. 2009, *A&A*, 494, 1083
- Aoki, W., Beers, T. C., Christlieb, N., et al. 2007, *ApJ*, 655, 492
- Aoki, W., Ryan, S. G., Norris, J. E., et al. 2002, *ApJ*, 580, 1149
- Aoki, W., Honda, S., Beers, T. C., et al. 2005, *ApJ*, 632, 611
- Aoki, W., Frebel, A., Christlieb, N., et al. 2006, *ApJ*, 639, 897
- Aoki, W., Beers, T. C., Sivarani, T., et al. 2008, *ApJ*, 678, 1351
- Aoki, W., Beers, T. C., Lee, Y. S., et al. 2013, *AJ*, 145, 13
- Arcones, A., & Thielemann, F. K. 2013, *Journal of Physics G Nuclear Physics*, 40, 013201
- Arentsen, A., Starkenburg, E., Shetrone, M. D., et al. 2019a, *A&A*, 621, A108
- Arentsen, A., Prugniel, P., Gonneau, A., et al. 2019b, *A&A*, 627, A138
- Argast, D., Samland, M., Thielemann, F. K., & Qian, Y. Z. 2004, *A&A*, 416, 997
- Asplund, M., Grevesse, N., Sauval, A. J., & Scott, P. 2009, *ARA&A*, 47, 481
- Barklem, P. S., & O'Mara, B. J. 2000, *MNRAS*, 311, 535
- Bartkevicius, A. 1996, *Baltic Astronomy*, 5, 217
- Beers, T. C. 1999, in *Astronomical Society of the Pacific Conference Series*, Vol. 165, *The Third Stromlo Symposium: The Galactic Halo*, ed. B. K. Gibson, R. S. Axelrod, & M. E. Putman, 202
- Beers, T. C., & Christlieb, N. 2005, *ARA&A*, 43, 531
- Beers, T. C., Preston, G. W., & Shectman, S. A. 1985, *AJ*, 90, 2089
- . 1992, *AJ*, 103, 1987
- Beers, T. C., Flynn, C., Rossi, S., et al. 2007, *ApJS*, 168, 128
- Bensby, T., Feltzing, S., & Lundström, I. 2003, *A&A*, 410, 527
- . 2004, *A&A*, 415, 155
- Bergemann, M., Hansen, C. J., Bautista, M., & Ruchti, G. 2012, *A&A*, 546, A90
- Bertolli, M. G., Herwig, F., Pignatari, M., & Kawano, T. 2013, *arXiv e-prints*, arXiv:1310.4578
- Bessell, M. S., Collet, R., Keller, S. C., et al. 2015, *ApJL*, 806, L16
- Bisterzo, S., Gallino, R., Straniero, O., Cristallo, S., & Käppeler, F. 2010, *MNRAS*, 404, 1529
- . 2011, *MNRAS*, 418, 284
- Bonifacio, P., Caffau, E., Spite, M., et al. 2015, *A&A*, 579, A28
- Busso, M., Gallino, R., Lambert, D. L., Travaglio, C., & Smith, V. V. 2001, *ApJ*, 557, 802
- Campbell, S. W., & Lattanzio, J. C. 2008, *A&A*, 490, 769
- Campbell, S. W., Lugaro, M., & Karakas, A. I. 2010, *A&A*, 522, L6
- Carollo, D., Beers, T. C., Bovy, J., et al. 2012, *ApJ*, 744, 195
- Cayrel, R., Depagne, E., Spite, M., et al. 2004, *A&A*, 416, 1117
- Charbonnel, C. 1995, *ApJL*, 453, L41
- Charbonnel, C., Brown, J. A., & Wallerstein, G. 1998, *A&A*, 332, 204
- Chen, B., Vergely, J. L., Valette, B., & Carraro, G. 1998, *A&A*, 336, 137
- Chiappini, C. 2013, *Astronomische Nachrichten*, 334, 595
- Choplin, A., Hirschi, R., Meynet, G., & Ekström, S. 2017, *A&A*, 607, L3
- Christlieb, N. 2003, *Reviews in Modern Astronomy*, 16, 191
- Christlieb, N., Green, P. J., Wisotzki, L., & Reimers, D. 2001a, *A&A*, 375, 366
- Christlieb, N., Schörck, T., Frebel, A., et al. 2008, *A&A*, 484, 721
- Christlieb, N., Wisotzki, L., Reimers, D., et al. 2001b, *A&A*, 366, 898
- Clayton, D. D. 1988, *MNRAS*, 234, 1
- Cooke, R. J., & Madau, P. 2014, *ApJ*, 791, 116
- Cowan, J. J., & Rose, W. K. 1977, *ApJ*, 212, 149

- Cristallo, S., Karinkuzhi, D., Goswami, A., Piersanti, L., & Gobrecht, D. 2016, *ApJ*, 833, 181
- Cristallo, S., Straniero, O., Gallino, R., et al. 2009, *ApJ*, 696, 797
- Cristallo, S., Straniero, O., Piersanti, L., & Gobrecht, D. 2015, *ApJS*, 219, 40
- Cristallo, S., Piersanti, L., Straniero, O., et al. 2011, *ApJS*, 197, 17
- Cruz, M. A., Serenelli, A., & Weiss, A. 2013, *A&A*, 559, A4
- Cseh, B., Lugaro, M., D’Orazi, V., et al. 2018, *A&A*, 620, A146
- Cui, X.-Q., Zhao, Y.-H., Chu, Y.-Q., et al. 2012, *Research in Astronomy and Astrophysics*, 12, 1197
- Dardelet, L., Ritter, C., Prado, P., et al. 2014, in *XIII Nuclei in the Cosmos (NIC XIII)*, 145
- de Castro, D. B., Pereira, C. B., Roig, F., et al. 2016, *MNRAS*, 459, 4299
- Deng, L.-C., Newberg, H. J., Liu, C., et al. 2012, *Research in Astronomy and Astrophysics*, 12, 735
- Denissenkov, P. A., Herwig, F., Battino, U., et al. 2017, *ApJL*, 834, L10
- Denissenkov, P. A., Herwig, F., Woodward, P., et al. 2019, *MNRAS*, 488, 4258
- Doherty, C. L., Gil-Pons, P., Siess, L., Lattanzio, J. C., & Lau, H. H. B. 2015, *MNRAS*, 446, 2599
- Drout, M. R., Piro, A. L., Shappee, B. J., et al. 2017, *Science*, 358, 1570
- Frebel, A. 2018, *Annual Review of Nuclear and Particle Science*, 68, 237
- Frebel, A., Collet, R., Eriksson, K., Christlieb, N., & Aoki, W. 2008, *ApJ*, 684, 588
- Frebel, A., & Norris, J. E. 2015, *ARA&A*, 53, 631
- Fryer, C. L., Herwig, F., Hungerford, A., & Timmes, F. X. 2006, *ApJL*, 646, L131
- Fujimoto, M. Y., Ikeda, Y., & Iben, Icko, J. 2000, *ApJL*, 529, L25
- Gaia Collaboration, Katz, D., Antoja, T., et al. 2018, *A&A*, 616, A11
- Gallino, R., Bisterzo, S., Husti, L., et al. 2006, in *International Symposium on Nuclear Astrophysics - Nuclei in the Cosmos*, ed. A. Mengoni, J. Cederkall, J. D’Auria, L. Fraile, H. Fynbo, M. Hass, M. M. Jeanne, M. Hjorth Jensen, F. Kaeppler, K. L. Kratz, M. Lindroos, M. Menna, G. Meynet, & K. Riisager, 100.1
- García-Hernández, D. A., García-Lario, P., Plez, B., et al. 2006, *Science*, 314, 1751
- . 2007, *A&A*, 462, 711
- García-Hernández, D. A., Manchado, A., Lambert, D. L., et al. 2009, *ApJL*, 705, L31
- Gilroy, K. K. 1989, *ApJ*, 347, 835
- Girardi, L., Bressan, A., Bertelli, G., & Chiosi, C. 2000, *A&AS*, 141, 371
- Goriely, S., & Mowlavi, N. 2000, *A&A*, 362, 599
- Goriely, S., & Siess, L. 2005, in *From Lithium to Uranium: Elemental Tracers of Early Cosmic Evolution*, ed. V. Hill, P. Francois, & F. Primas, Vol. 228, 451–460
- Goswami, A., & Aoki, W. 2010, *MNRAS*, 404, 253
- Goswami, A., Aoki, W., Beers, T. C., et al. 2006, *MNRAS*, 372, 343
- Goswami, A., Aoki, W., & Karinkuzhi, D. 2016, *MNRAS*, 455, 402
- Goswami, P. P., Rathour, R. S., & Goswami, A. 2021, *A&A*, 649, A49
- Gratton, R. G., Sneden, C., Carretta, E., & Bragaglia, A. 2000, *A&A*, 354, 169
- Grundahl, F., Briley, M., Nissen, P. E., & Feltzing, S. 2002, *A&A*, 385, L14
- Hempel, M., Karakas, A. I., Stancliffe, R. J., Meyer, B. S., & Lugaro, M. 2019, *ApJ*, 887, 11
- Hempel, M., Stancliffe, R. J., Lugaro, M., & Meyer, B. S. 2016, *ApJ*, 831, 171
- Hansen, C. J., Hansen, T. T., Koch, A., et al. 2019, *A&A*, 623, A128
- Hansen, C. J., Nordström, B., Hansen, T. T., et al. 2016a, *A&A*, 588, A37
- Hansen, T., Andersen, J., Nordström, B., Buchhave, L. A., & Beers, T. C. 2011, *ApJL*, 743, L1
- Hansen, T., Hansen, C. J., Christlieb, N., et al. 2015a, *ApJ*, 807, 173
- . 2015b, *ApJ*, 807, 173
- Hansen, T. T., Andersen, J., Nordström, B., et al. 2016b, *A&A*, 588, A3
- Heger, A., & Woosley, S. E. 2010, *ApJ*, 724, 341
- Herwig, F. 2005, *ARA&A*, 43, 435
- Herwig, F., Pignatari, M., Woodward, P. R., et al. 2011, *ApJ*, 727, 89
- Herwig, F., Woodward, P. R., Lin, P.-H., Knox, M., & Fryer, C. 2014, *ApJL*, 792, L3
- Hollek, J. K., Frebel, A., Placco, V. M., et al. 2015, *ApJ*, 814, 121
- Honda, S., Aoki, W., Kajino, T., et al. 2004, *ApJ*, 607, 474
- Husti, L., Gallino, R., Bisterzo, S., Straniero, O., & Cristallo, S. 2009, *PASA*, 26, 176
- Iwamoto, N., Umeda, H., Tominaga, N., Nomoto, K., & Maeda, K. 2005, *Science*, 309, 451
- Jacobson, H. R., Pilachowski, C. A., & Friel, E. D. 2005, in *American Astronomical Society Meeting Abstracts*, Vol. 207, American Astronomical Society Meeting Abstracts, 71.16
- Johnson, D. R. H., & Soderblom, D. R. 1987, *AJ*, 93, 864

- Jones, S., Ritter, C., Herwig, F., et al. 2016, *MNRAS*, 455, 3848
- Jonsell, K., Barklem, P. S., Gustafsson, B., et al. 2006, *A&A*, 451, 651
- Jorissen, A., Van Eck, S., Van Winckel, H., et al. 2016, *A&A*, 586, A158
- Karakas, A. I. 2010, *MNRAS*, 403, 1413
- Karakas, A. I., García-Hernández, D. A., & Lugaro, M. 2012, *ApJ*, 751, 8
- Karakas, A. I., & Lattanzio, J. C. 2003, *PASA*, 20, 279
- . 2014, *PASA*, 31, e030
- Karinkuzhi, D., & Goswami, A. 2014, *MNRAS*, 440, 1095
- . 2015, *MNRAS*, 446, 2348
- Karinkuzhi, D., Van Eck, S., Goriely, S., et al. 2021, *A&A*, 645, A61
- Karinkuzhi, D., Van Eck, S., Jorissen, A., et al. 2018, *A&A*, 618, A32
- Keenan, P. C. 1942, *ApJ*, 96, 101
- Koch, A., Reichert, M., Hansen, C. J., et al. 2019, *A&A*, 622, A159
- Lambert, D. L., & Luck, R. E. 1976, *The Observatory*, 96, 100
- Lambert, D. L., Smith, V. V., Busso, M., Gallino, R., & Straniero, O. 1995, *ApJ*, 450, 302
- Lattanzio, J., Frost, C., Cannon, R., & Wood, P. R. 1996, *Mem. Soc. Astron. Italiana*, 67, 729
- Lau, H. H. B., Stancliffe, R. J., & Tout, C. A. 2009, *MNRAS*, 396, 1046
- Lawler, J. E., Bonvallet, G., & Sneden, C. 2001, *ApJ*, 556, 452
- Lee, Y. S., Beers, T. C., Masseron, T., et al. 2013, *AJ*, 146, 132
- Lippuner, J., Fernández, R., Roberts, L. F., et al. 2017, *MNRAS*, 472, 904
- Lucatello, S., Beers, T. C., Christlieb, N., et al. 2006, *ApJL*, 652, L37
- Lucatello, S., Tsangarides, S., Beers, T. C., et al. 2005, *ApJ*, 625, 825
- Luck, R. E. 2017, *AJ*, 153, 21
- Luck, R. E., & Heiter, U. 2007, *AJ*, 133, 2464
- Maeder, A., & Meynet, G. 2015, *A&A*, 580, A32
- Maeder, A., Meynet, G., & Chiappini, C. 2015, *A&A*, 576, A56
- Mashonkina, L., Zhao, G., Gehren, T., et al. 2008, *A&A*, 478, 529
- Masseron, T., Johnson, J. A., Plez, B., et al. 2010, *A&A*, 509, A93
- McWilliam, A. 1998, *AJ*, 115, 1640
- Meynet, G., Hirschi, R., Ekstrom, S., et al. 2010, *A&A*, 521, A30
- Mishenina, T. V., Soubiran, C., Kovtyukh, V. V., & Korotin, S. A. 2004, *A&A*, 418, 551
- Mowlavi, N. 1999, *A&A*, 344, 617
- Noguchi, K., Aoki, W., Kawanomoto, S., et al. 2002, *PASJ*, 54, 855
- Nomoto, K., Kobayashi, C., & Tominaga, N. 2013, *ARA&A*, 51, 457
- Norris, J. E., Bessell, M. S., Yong, D., et al. 2013a, *ApJ*, 762, 25
- Norris, J. E., Yong, D., Bessell, M. S., et al. 2013b, *ApJ*, 762, 28
- Placco, V. M., Frebel, A., Beers, T. C., et al. 2013, *ApJ*, 770, 104
- Placco, V. M., Frebel, A., Beers, T. C., & Stancliffe, R. J. 2014, *ApJ*, 797, 21
- Placco, V. M., Sneden, C., Roederer, I. U., et al. 2021, *Research Notes of the American Astronomical Society*, 5, 92
- Plez, B., Smith, V. V., & Lambert, D. L. 1993, *ApJ*, 418, 812
- Prochaska, J. X., & McWilliam, A. 2000, *ApJL*, 537, L57
- Prochaska, J. X., Naumov, S. O., Carney, B. W., McWilliam, A., & Wolfe, A. M. 2000, *AJ*, 120, 2513
- Purandardas, M., Goswami, A., Goswami, P. P., Shejeelammal, J., & Masseron, T. 2019, *MNRAS*, 486, 3266
- Qian, Y. Z. 2000, *ApJL*, 534, L67
- Reddy, B. E., Lambert, D. L., & Allende Prieto, C. 2006, *MNRAS*, 367, 1329
- Rossi, S., Beers, T. C., & Sneden, C. 1999, in *Astronomical Society of the Pacific Conference Series*, Vol. 165, *The Third Stromlo Symposium: The Galactic Halo*, ed. B. K. Gibson, R. S. Axelrod, & M. E. Putman, 264
- Rosswog, S., Korobkin, O., Arcones, A., Thielemann, F. K., & Piran, T. 2014, *MNRAS*, 439, 744
- Schönrich, R., Binney, J., & Dehnen, W. 2010, *MNRAS*, 403, 1829
- Shejeelammal, J., Goswami, A., Goswami, P. P., Rathour, R. S., & Masseron, T. 2020, *MNRAS*, 492, 3708
- Shejeelammal, J., Goswami, A., & Shi, J. 2021, *MNRAS*, 502, 1008
- Shetrone, M. D. 2003, *ApJL*, 585, L45
- Short, C. I., & Hauschildt, P. H. 2006, *ApJ*, 641, 494
- Skúladóttir, Á., Tolstoy, E., Salvadori, S., et al. 2015, *A&A*, 574, A129
- Sneden, C. A. 1973, PhD thesis, THE UNIVERSITY OF TEXAS AT AUSTIN.
- Sperauskas, J., Začs, L., Schuster, W. J., & Deveikis, V. 2016, *ApJ*, 826, 85

- Spite, M., Caffau, E., Bonifacio, P., et al. 2013, *A&A*, 552, A107
- Spite, M., Cayrel, R., Plez, B., et al. 2005, *A&A*, 430, 655
- Spite, M., Cayrel, R., Hill, V., et al. 2006, *A&A*, 455, 291
- Stancliffe, R. J., Dearborn, D. S. P., Lattanzio, J. C., Heap, S. A., & Campbell, S. W. 2011, *ApJ*, 742, 121
- Starkenburger, E., Shetrone, M. D., McConnachie, A. W., & Venn, K. A. 2014, *MNRAS*, 441, 1217
- Sugimoto, D. 1971, *Progress of Theoretical Physics*, 45, 761
- Surman, R., McLaughlin, G. C., Ruffert, M., Janka, H. T., & Hix, W. R. 2008, *ApJL*, 679, L117
- Tanvir, N. R., Levan, A. J., Fruchter, A. S., et al. 2013, *Nature*, 500, 547
- Tominaga, N., Iwamoto, N., & Nomoto, K. 2014, *ApJ*, 785, 98
- Tominaga, N., Umeda, H., & Nomoto, K. 2007, *ApJ*, 660, 516
- Umeda, H., & Nomoto, K. 2005, *ApJ*, 619, 427
- van Raai, M. A., Lugaro, M., Karakas, A. I., García-Hernández, D. A., & Yong, D. 2012, *A&A*, 540, A44
- Vanture, A. D. 1992, *AJ*, 104, 1997
- Venn, K. A., Irwin, M., Shetrone, M. D., et al. 2004, *AJ*, 128, 1177
- Ventura, P., & D'Antona, F. 2005, *A&A*, 431, 279
- Vernet, J., Dekker, H., D'Odorico, S., et al. 2011, *A&A*, 536, A105
- Wallerstein, G., Iben, Icko, J., Parker, P., et al. 1997, *Reviews of Modern Physics*, 69, 995
- Woodward, P. R., Herwig, F., & Lin, P.-H. 2015, *ApJ*, 798, 49
- Worley, C. C., Hill, V., Sobeck, J., & Carretta, E. 2013, *A&A*, 553, A47
- Yamashita, Y. 1975, *PASJ*, 27, 325
- Yang, G.-C., Liang, Y.-C., Spite, M., et al. 2016, *Research in Astronomy and Astrophysics*, 16, 19
- Yong, D., Norris, J. E., Bessell, M. S., et al. 2013, *ApJ*, 762, 27
- Yoon, J., Beers, T. C., Placco, V. M., et al. 2016, *ApJ*, 833, 20
- York, D. G., Adelman, J., Anderson, John E., J., et al. 2000, *AJ*, 120, 1579
- Zhao, G., Zhao, Y.-H., Chu, Y.-Q., Jing, Y.-P., & Deng, L.-C. 2012, *Research in Astronomy and Astrophysics*, 12, 723

## APPENDIX

## A. LINELIST

**Table A1.** Equivalent widths (in mÅ) of Fe lines used for deriving atmospheric parameters.

Wavelength(Å)	El	$E_{low}$ (eV)	log gf	BD-19 132	BD-19 290	HE 1157-0518	HE 1304-2111	HE 1354-2257	BD+19 3109	HD 202851
4445.471	Fe I	0.087	-5.38	105.3(5.69)	34.9(4.75)	-	-	-	-	77.1(6.64)
4466.551		2.832	-0.59	-	-	-	-	-	-	136.4(6.59)
4484.22		3.603	-0.72	-	-	-	41.8(5.26)	-	-	-
4489.739		0.121	-3.966	-	-	-	-	108.3(5.31)	-	128.3(6.53)
4595.358		3.301	-1.72	56.0(5.73)	-	-	-	-	-	-
4619.288		3.603	-1.12	63.5(5.65)	-	-	-	-	-	87.3(6.79)
4625.045		3.241	-1.34	-	20.3(4.64)	-	36.6(5.25)	-	-	-
4630.12		2.278	-2.6	-	-	-	28.4(5.03)	50.1(5.66)	-	-
4635.846		2.845	-2.42	48.0(5.68)	-	-	-	-	24.0(5.17)	57.2(6.57)
4637.503		3.283	-1.39	69.5(5.59)	-	-	-	-	-	-
4643.464		3.654	-1.29	53.4(5.73)	-	-	-	-	38.2(5.40)	-
4787.827		2.998	-2.77	-	-	-	-	-	-	39.4(6.77)
4788.751		3.236	-1.81	52.5(5.61)	-	-	-	-	-	-
4789.651		3.546	-0.91	-	-	-	-	33.0(5.20)	-	-
4924.77		2.278	-2.22	-	-	22.1(5.20)	52.7(5.32)	48.8(5.26)	-	-
4930.315		3.959	-1.35	-	-	-	-	-	-	44.7(6.53)
4939.687		0.859	-3.34	-	128.5(4.67)	-	-	99.7(5.33)	-	-
4967.89		4.191	-0.622	-	-	-	-	-	35.5(5.38)	-
4985.253		3.93	-0.56	76.8(5.73)	-	-	-	-	-	96.6(6.75)
5001.863		3.882	0.01	-	-	32.8(4.84)	-	78.9(5.33)	-	-
5028.126		3.573	-1.474	41.8(5.59)	-	-	-	-	-	-
5044.211		2.851	-2.15	63.3(5.62)	-	-	-	22.3(5.36)	-	-
5049.819		2.278	-1.42	-	-	-	76.5(5.17)	-	-	-
5079.223		2.2	-2.067	-	-	27.9(5.04)	-	-	-	112.6(6.54)
5083.338		0.958	-2.958	-	-	-	81.4(5.11)	-	-	-
5127.359		0.915	-3.307	-	-	32.8(4.89)	-	-	-	-
5141.739		2.424	-2.15	-	-	-	-	-	78.1(5.14)	-
5151.911		1.011	-3.32	-	107.8(4.63)	-	-	-	-	-
5198.711		2.222	-2.135	-	-	-	-	58.3(5.18)	112.4(5.37)	-
5215.179		3.266	-0.933	102.6(5.61)	-	-	-	-	91.7(5.31)	113.3(6.67)
5242.491		3.634	-0.84	-	20.1(4.71)	-	-	46.0(5.54)	58.2(5.33)	94.3(6.71)
5247.05		0.087	-4.946	139.3(5.64)	66.8(4.60)	-	55.6(5.01)	-	124.1(5.23)	115.2(6.79)
5250.209		0.121	-4.938	-	58.7(4.52)	-	-	-	131.2(5.37)	-
5263.305		3.265	-0.97	-	-	-	44.7(5.05)	75.5(5.55)	-	-
5281.79		3.038	-1.02	-	-	41.2(4.96)	-	-	-	-
5322.04		2.28	-2.84	72.0(5.57)	-	-	-	-	47.9(5.14)	68.9(6.42)
5339.93		3.27	-0.68	-	-	55.0(5.26)	-	-	100.9(5.19)	-
5365.399		3.573	-1.44	43.2(5.57)	-	-	-	-	-	-
5367.479		4.415	0.35	-	34.7(4.66)	-	44.5(5.21)	-	69.9(5.25)	111.4(6.66)
5369.961		4.37	0.35	87.1(5.58)	30.8(4.54)	-	-	-	80.2(5.36)	100.9(6.38)
5383.369		4.312	0.5	-	-	-	-	-	80.7(5.13)	131.2(6.78)
5445.042		4.39	-0.02	73.5(5.75)	-	-	27.6(5.07)	-	43.6(5.16)	98.2(6.70)
5569.62		3.42	-0.49	-	-	-	-	99.8(5.67)	-	125.6(6.64)
5576.09		3.43	-0.851	-	-	-	-	-	68.4(5.21)	-
5586.756		3.368	-0.21	137.8(5.60)	-	-	68.9(5.10)	-	-	152.1(6.75)
5615.644		3.332	-0.14	-	-	-	-	-	129.0(5.31)	-
5701.544		2.559	-2.216	-	-	-	-	52.1(5.54)	80.1(5.37)	-
5753.12		4.26	-0.76	-	-	-	-	-	23.1(5.33)	67.6(6.65)
5883.813		3.959	-1.36	-	-	-	-	-	-	57.6(6.71)
5956.692		0.859	-4.605	-	-	-	38.9(5.22)	-	-	86.5(6.69)
6024.049		4.548	-0.12	-	-	-	-	-	35.7(5.30)	86.0(6.65)
6082.71		2.222	-3.573	-	-	-	-	-	21.7(5.29)	57.5(6.83)
6137.694		2.588	-1.403	-	105.3(4.73)	-	-	98.6(5.39)	135.7(5.38)	-
6151.62		2.18	-3.29	-	-	-	20.4(5.24)	21.3(5.57)	39.1(5.30)	-
6173.34		2.22	-2.88	-	-	-	-	30.6(5.41)	-	-
6200.314		2.608	-2.437	-	-	-	-	36.6(5.54)	-	-
6219.279		2.198	-2.433	-	-	25.2(5.27)	-	-	-	-
6240.646		2.222	-3.38	-	-	-	-	27.9(5.64)	-	-
6246.318		3.603	-0.96	75.7(5.60)	-	-	-	-	-	-
6252.554		2.404	-1.687	-	87.3(4.60)	46.9(5.12)	-	82.5(5.19)	-	-
6254.258		2.279	-2.48	-	-	-	-	73.6(5.62)	-	-
6280.617		0.859	-4.39	-	-	-	52.1(5.26)	-	-	-
6301.5		3.654	-0.672	-	-	-	37.6(5.06)	-	69.6(5.24)	101.8(6.51)
6318.018		2.453	-2.33	-	-	-	-	41.2(5.31)	83.7(5.32)	-
6322.69		2.588	-2.426	-	-	-	-	33.1(5.44)	-	-
6335.328		2.198	-2.23	-	-	-	-	58.7(5.14)	105.0(5.15)	127.5(6.69)
6336.823		3.686	-1.05	-	-	-	-	22.9(5.19)	-	-
6393.602		2.432	-1.62	-	-	-	-	90.4(5.25)	-	-
6416.933		4.796	-0.885	-	-	-	-	-	-	29.9(6.65)

The numbers in the parenthesis in columns 5 - 11 give the derived abundances from the respective line.

Wavelength(Å)	El	$E_{low}$ (eV)	log gf	BD-19 132	BD-19 290	HE 1157-0518	HE 1304-2111	HE 1354-2257	BD+19 3109	HD 202851
6421.349		2.278	-2.027	-	-	-	65.9(5.21)	80.7(5.32)	-	-
6430.85		2.18	-2.01	-	-	-	-	107.9(5.55)	-	-
6575.019		2.588	-2.82	52.0(5.67)	-	-	-	-	-	62.4(6.58)
6592.91		2.72	-1.47	-	57.0(4.62)	-	-	56.6(5.12)	95.8(5.13)	124.5(6.61)
6593.871		2.432	-2.422	-	-	-	-	-	-	105.1(6.71)
6677.989		2.692	-1.47	-	-	45.0(5.17)	-	-	-	-
4491.405	Fe II	2.855	-2.7	-	-	-	-	33.7(5.21)	22.8(5.29)	-
4508.288		2.855	-2.21	45.0(5.64)	29.5(4.55)	25.2(4.97)	-	-	40.4(5.27)	-
4515.339		2.84	-2.48	-	-	-	-	-	30.3(5.26)	-
4520.224		2.81	-2.6	32.7(5.65)	-	-	-	-	-	-
4629.339		2.807	-2.28	-	-	-	31.5(5.16)	-	-	-
4731.453		2.891	-3.36	-	-	-	-	20.5(5.58)	-	-
5197.56		3.23	-2.25	-	-	-	24.0(5.23)	-	-	85.4(6.62)
5234.62		3.22	-2.24	-	25.4(4.73)	25.4(5.20)	22.0(5.09)	52.3(5.35)	-	-
5534.83		3.25	-2.77	-	-	-	-	-	-	48.3(6.64)
6247.55		3.89	-2.34	-	-	-	-	-	-	46.4(6.72)
6456.383		3.903	-2.075	-	-	-	-	19.9(5.40)	-	-

The numbers in the parenthesis in columns 5 - 11 give the derived abundances from the respective line. The line information are taken from Kurucz database of atomic line lists (<https://lweb.cfa.harvard.edu/amp/ampdata/kurucz23/sekur.html>).

**Table A2.** Equivalent widths (in mÅ) of lines used for deriving elemental abundances.

Wavelength(Å)	El	$E_{low}$ (eV)	log gf	BD-19 132	BD-19 290	HE 1157-0518	HE 1304-2111	HE 1354-2257	BD+19 3109	HD 202851
5682.633	Na I	2.102	-0.7	120.0(5.52)	31.5(4.65)	-	129.8(6.65)	27.3(4.76)	21.5(4.14)	93.0(5.90)
5688.205		2.1	-0.45	130.5(5.42)	35.4(4.47)	-	170.5(6.81)	35.5(4.67)	31.8(4.11)	104.3(5.84)
6160.747		2.104	-1.26	-	-	-	-	-	-	66.4(6.00)
4702.991	Mg I	4.346	-0.666	-	-	-	-	-	115.9(6.05)	151.9(6.95)
4730.029		4.346	-2.523	37.1(6.30)	-	-	-	-	28.4(6.29)	-
5528.405		4.346	-0.62	-	89.4(5.35)	67.0(5.45)	68.5(5.46)	-	141.5(6.06)	171.8(7.09)
5711.088		4.346	-1.833	92.4(6.33)	-	-	-	12.4(5.47)	-	-
5948.541	Si I	5.083	-1.23	-	110.0(6.99)	-	24.8(5.91)	25.7(6.01)	-	90.8(6.63)
6237.319		5.613	-0.53	-	98.7(6.80)	-	27.0(5.92)	20.2(5.78)	-	-
4425.437	Ca I	1.879	-0.385	-	-	66.0(4.60)	-	-	-	-
4435.679		1.89	-0.52	-	57.8(4.00)	-	-	-	-	-
4455.887		1.899	-0.51	-	-	38.8(4.03)	-	-	-	-
5265.56		2.52	-0.11	-	40.4(3.90)	-	50.3(4.38)	-	-	-
5581.965		2.523	-1.833	116.9(5.13)	-	-	-	-	56.7(4.36)	-
5590.114		2.521	-0.71	-	-	12.4(4.22)	-	23.1(4.38)	47.4(4.21)	74.6(5.43)
5594.462		2.523	-0.05	-	58.7(3.89)	31.8(3.91)	-	-	-	-
5857.451		2.932	0.23	-	-	-	-	44.9(4.35)	59.7(4.01)	94.5(5.34)
6102.723		1.879	-0.89	-	-	-	-	53.4(4.35)	98.2(4.12)	115.9(5.63)
6162.173		1.899	0.1	-	137.6(3.92)	-	-	105.7(4.34)	-	-
6166.439		2.521	-0.9	-	-	-	-	-	37.5(4.16)	72.1(5.54)
6169.042		2.523	-0.55	-	-	-	-	36.2(4.47)	-	-
6169.563		2.523	-0.27	-	-	-	-	-	-	96.0(5.37)
6439.075		2.525	0.47	-	-	-	-	103.7(4.66)	137.5(4.24)	155.9(5.61)
6449.808		2.523	-0.55	138.0(5.12)	-	-	-	-	-	92.6(5.55)
6471.662		2.525	-0.59	152.7(5.36)	-	-	-	42.9(4.62)	68.0(4.28)	-
6493.781		2.521	0.14	-	-	69.1(4.12)	-	-	-	112.0(5.23)
4453.312	Ti I	1.43	-0.051	-	-	-	-	-	-	59.2(4.34)
4533.239		0.848	0.476	-	-	-	-	62.2(2.60)	-	-
4617.269		1.749	0.389	-	-	-	-	-	-	81.0(4.25)
4778.255		2.24	-0.22	-	-	-	-	-	-	38.1(4.54)
4820.41		1.503	-0.441	-	-	-	25.4(3.17)	-	-	-
4840.874		0.899	-0.509	163.9(3.80)	-	-	-	-	-	89.1(4.27)
4926.147		0.818	-2.17	78.8(3.83)	-	-	-	-	-	-
4999.5		0.83	0.31	-	-	28.4(2.36)	82.8(3.13)	-	-	133.6(4.31)
5024.842		0.818	-0.602	-	-	-	-	-	-	94.3(4.33)
5039.96		0.02	-1.13	-	68.4(2.32)	-	-	-	-	104.5(4.12)
5210.386		0.047	-0.884	-	84.8(2.24)	-	77.6(2.90)	-	-	-
5471.197		1.443	-1.44	-	-	-	-	-	32.6(3.45)	-
5739.982		2.236	-0.67	-	-	-	-	-	-	23.6(4.62)
5918.535		1.07	-1.46	103.4(3.64)	-	-	-	-	-	36.6(4.30)
5922.11		1.046	-1.466	95.3(3.50)	-	-	-	-	-	45.0(4.44)
5937.811		1.067	-1.89	-	-	-	-	-	38.6(3.36)	-
5941.751		1.05	-1.51	95.8(3.56)	-	-	-	-	-	31.7(4.24)

The numbers in the parenthesis in columns 5 - 11 give the derived abundances from the respective line.

Wavelength(Å)	El	$E_{low}$ (eV)	log gf	BD-19 132	BD-19 290	HE 1157-0518	HE 1304-2111	HE 1354-2257	BD+19 3109	HD 202851
5965.828		1.879	-0.409	-	-	-	-	-	57.0(3.38)	-
5978.543		1.873	-0.496	-	-	-	-	-	52.6(3.39)	-
6064.629		1.046	-1.944	-	-	-	-	-	-	26.8(4.56)
6303.757		1.443	-1.566	-	-	-	-	-	43.5(3.64)	-
6556.062		1.46	-1.074	89.1(3.59)	-	-	-	-	-	42.5(4.45)
6599.133		0.9	-2.085	-	-	-	-	-	60.2(3.49)	-
4161.535	Ti II	1.084	-2.36	-	-	-	-	-	-	92.8(4.35)
4443.794		1.08	-0.7	-	-	-	-	-	-	157.1(4.15)
4493.51		1.08	-2.73	60.0(3.34)	-	-	-	-	-	-
4563.761		1.22	-0.96	139.8(3.33)	114.3(2.20)	-	-	-	124.4(3.00)	-
4568.314		1.22	-2.65	61.1(3.47)	-	-	-	-	42.1(3.03)	-
4571.96		1.571	-0.53	123.1(4.73)	-	-	-	-	-	-
4636.32		1.164	-2.855	-	-	-	-	-	-	67.0(4.42)
4708.665		1.236	-2.21	-	-	-	-	-	-	86.9(4.29)
4764.526		1.236	-2.77	62.0(3.57)	-	-	-	22.2(2.80)	-	76.8(4.61)
4779.985		2.048	-1.37	-	20.9(2.16)	18.3(2.75)	-	-	57.0(3.14)	97.5(4.64)
4798.521		1.08	-2.43	-	296(2.14)	-	-	42.2(2.68)	-	82.4(4.21)
4805.085		2.061	-1.1	87.9(3.56)	-	-	33.2(2.54)	-	-	-
4865.612		1.116	-2.61	73.7(3.43)	-	-	-	31.8(2.70)	-	80.6(4.38)
5185.9		1.89	-1.35	-	-	21.8(2.61)	99.50(5.36)	48.4(2.64)	87.2(3.32)	-
5226.543		1.566	-1.3	-	-	32.1(2.42)	-	-	-	-
5336.771		1.58	-1.7	81.4(3.23)	-	-	-	-	-	107.4(4.56)
5381.015		1.566	-2.08	-	-	-	-	-	69.9(3.20)	-
5418.751		1.581	-1.999	-	50.8(4.42)	-	-	-	-	-
4351.05	Cr I	0.97	-1.45	-	-	17.3(3.26)	-	-	-	-
4600.748		1.004	-1.26	-	-	-	87.0(4.52)	-	-	-
4626.173		0.968	-1.32	-	-	-	-	-	73.7(2.71)	-
4737.347		3.087	-0.099	-	-	-	29.9(4.29)	-	-	73.5(5.31)
4829.372		2.544	-0.81	-	-	-	-	-	-	58.8(5.08)
4870.801		3.079	0.05	-	-	-	42.0(4.51)	-	-	-
4942.49		0.941	-2.294	-	-	-	-	-	33.9(2.91)	99.5(5.55)
5247.565		0.961	-1.64	-	-	-	-	-	77.3(2.86)	-
5296.691		0.982	-1.4	-	-	-	-	-	-	114.3(5.18)
5298.277		0.983	-1.15	-	-	-	100.0(4.39)	-	-	125.6(5.19)
5300.744		0.982	-2.12	-	-	-	-	-	46.1(2.92)	-
5312.871		3.45	-0.562	-	-	-	-	-	-	28.6(5.23)
5345.801		1.003	-0.98	-	-	-	-	-	122.9(2.91)	145.7(5.16)
5348.312		1.003	-1.29	-	-	18.8(3.10)	-	-	95.6(2.81)	-
5409.772		1.03	-0.72	-	-	-	-	-	125.4(2.70)	168.4(5.25)
5787.965		3.323	-0.083	-	-	-	-	-	-	65.9(5.32)
4634.07	Cr II	4.072	-1.24	-	25.9(3.87)	-	-	44.6(4.24)	-	-
4812.337		3.864	-1.8	-	39.4(3.73)	-	-	-	-	-
4848.25		3.864	-1.14	-	-	-	-	35.9(4.36)	-	-
5305.853		3.827	-2.357	-	-	-	-	-	-	36.1(5.40)
5308.404		4.072	-1.81	-	-	-	-	-	-	37.8(5.16)
5334.869		4.073	-1.562	-	-	-	-	-	-	43.5(5.04)
4470.472	Ni I	3.399	-0.31	30.8(4.19)	-	-	-	-	-	-
4686.207		3.597	-0.64	-	-	-	-	-	44.7(4.59)	75.0(5.77)
4703.803		3.658	-0.735	-	-	-	-	-	-	-
4714.408		3.38	0.23	-	-	-	-	30.5(3.59)	-	-
4731.793		3.833	-0.85	-	-	-	-	-	-	61.0(5.92)
4752.415		3.658	-0.7	-	-	-	-	-	-	76.4(5.91)
4756.51		3.48	-0.34	-	-	-	-	-	-	90.8(5.69)
4980.166		3.606	-0.11	-	-	-	28.10(4.00)	-	-	-
5035.357		3.635	0.29	78.9(4.21)	-	-	-	-	-	-
5081.107		3.847	0.3	52.8(4.02)	-	-	38.7(4.23)	-	-	-
5082.35		3.657	-0.54	-	-	-	32.2(4.06)	-	-	-
5084.089		3.678	0.03	75.0(4.45)	-	15.6(3.92)	-	20.7(3.87)	-	-
5099.927		3.678	-0.1	-	-	-	-	-	-	97.4(5.78)
5102.96		1.676	-2.62	-	44.9(4.07)	-	-	-	89.0(4.45)	-
5115.389		3.834	-0.11	-	-	11.7(4.09)	-	-	-	83.3(5.64)
5146.48		3.706	0.12	-	55.4(4.15)	-	-	-	-	-
6175.36		4.089	-0.53	-	-	-	-	-	-	52.0(5.64)
6176.807		4.088	-0.26	-	-	-	-	-	-	70.5(6.01)
6204.6		4.088	-1.13	-	-	-	-	-	-	31.3(5.82)
6327.593		1.676	-3.15	-	-	-	-	-	66.8(4.34)	75.7(5.84)
6378.247		4.154	-0.89	-	-	-	-	-	-	37.8(5.79)
6643.629		1.676	-2.3	-	102.2(4.14)	14.6(3.89)	61.3(4.31)	34.8(3.98)	-	-
4722.15	Zn I	4.029	-0.37	-	27.4(2.33)	-	-	29.9(2.50)	-	-
4810.53		4.08	-0.17	48.3(3.00)	-	-	-	-	29.6(2.48)	64.1(3.48)
4883.684	Y II	1.084	0.07	-	-	73.5(0.67)	-	-	-	169.0(2.97)
5087.416		1.084	-0.17	-	-	-	-	-	-	164.9(3.12)
5119.112		0.992	-1.36	-	-	-	-	-	89.2(1.55)	104.3(3.11)
5200.406		0.992	-1.36	-	-	35.5(0.55)	-	-	-	-

The numbers in the parenthesis in columns 5 - 11 give the derived abundances from the respective line.

Wavelength(Å)	El	$E_{low}$ (eV)	log gf	BD-19 132	BD-19 290	HE 1157-0518	HE 1304-2111	HE 1354-2257	BD+19 3109	HD 202851
5205.724		1.033	-0.34	-	-	41.8(0.48)	-	-	-	-
5289.815		1.033	-1.85	-	-	-	-	-	44.4(1.23)	78.2(2.99)
5402.774		1.839	-0.51	-	25.9(0.46)	-	-	-	-	-
5544.611		1.738	-1.09	101.0(2.64)	-	-	14.1(0.83)	-	-	-
5546.009		1.748	-1.11	-	-	-	-	-	-	-
5662.925		1.944	0.16	156.8(2.64)	52.7(0.31)	22.7(0.61)	-	-	-	-
6613.733		1.748	-1.1	123.5(2.85)	-	-	12.1(0.67)	-	54.5(1.47)	-
4739.48	Zr I	0.651	0.23	-	8.3(0.95)	-	30.9(1.80)	-	-	-
4772.323		0.623	0.04	-	8.3(1.10)	-	-	-	-	-
6134.585		0	-1.28	-	-	-	19.2(1.75)	-	-	-
4317.321	Zr II	0.713	-1.38	98.3(2.24)	-	-	-	-	53.7(1.28)	-
5112.297		1.665	-0.59	88.0(2.34)	-	-	-	-	-	-
4336.244	Ce II	0.704	-0.564	-	47.3(0.64)	-	-	-	-	-
4364.653		0.495	-0.201	-	-	-	-	-	94.5(1.08)	-
4407.273		0.701	-0.741	-	-	-	21.6(0.67)	-	-	-
4483.893		0.864	0.01	-	-	38.5(0.99)	-	-	-	-
4497.846		0.958	-0.349	-	-	-	-	48.2(1.11)	-	80.5(2.90)
4508.079		0.621	-1.238	-	-	-	-	-	36.1(1.04)	57.4(2.58)
4560.28		0.91	0	-	-	34.4(0.96)	-	-	-	-
4562.359		0.477	0.081	-	-	62.9(0.87)	-	97.8(1.20)	-	103.5(2.30)
4628.161		0.516	0.008	174.3(2.31)	-	-	-	-	105.1(0.95)	115.7(2.69)
4725.069		0.521	-1.204	-	32.1(0.65)	-	-	-	40.6(0.87)	-
4747.167		0.32	-1.246	-	-	-	-	-	53.7(0.86)	-
4773.941		0.924	-0.498	-	-	-	-	-	42.3(0.77)	-
4873.999		1.107	-0.892	-	-	-	12.5(0.84)	-	-	53.6(2.67)
5187.458		1.211	-0.104	-	60.9(0.78)	-	-	58.5(1.25)	-	82.9(2.68)
5274.229		1.044	-0.323	-	89.2(0.46)	62.2(1.19)	-	-	89.2(0.84)	-
5330.556		0.869	-0.76	103.2(2.06)	-	-	-	39.8(1.12)	-	70.9(2.60)
6034.205		1.458	-1.019	53.6(2.23)	-	-	-	-	-	35.2(2.74)
5188.217	Pr II	0.922	-1.145	53.4(1.52)	-	-	-	-	-	36.0(2.17)
5219.045		0.795	-0.24	112.1(1.47)	-	11.9(0.31)	21.3(-0.06)	24.0(0.06)	60.3(0.37)	-
5259.728		0.633	-0.682	93.4(1.30)	-	-	-	-	-	72.7(2.15)
5292.619		0.648	-0.3	-	53.1(-0.06)	10.8(0.15)	-	33.3(0.13)	54.5(0.10)	77.3(1.90)
5322.772		0.482	-0.315	-	55.9(-0.23)	12.4(0.04)	-	49.5(0.23)	79.3(0.28)	86.9(1.94)
6165.891		0.923	-0.205	-	-	8.70(0.21)	-	-	50.3(0.18)	-
4446.384	Nd II	0.204	-0.59	-	-	49.4(0.84)	-	-	93.6(0.75)	-
4451.563		0.38	-0.04	-	-	-	-	-	112.6(0.84)	119.8(2.52)
4556.133		0.064	-1.61	-	-	-	-	-	58.1(0.76)	-
4556.133		0.064	-1.61	123.1(2.14)	-	17.0(0.99)	-	-	-	-
4703.572		0.38	-1.07	-	58.8(0.50)	-	-	-	-	-
4706.543		0	-0.88	-	-	-	-	-	-	-
4797.153		0.559	-0.95	-	-	-	29.1(0.67)	41.7(0.82)	-	-
4811.342		0.064	-1.14	148.9(2.05)	90.7(0.50)	-	-	79.9(1.15)	85.3(0.68)	98.4(2.59)
4825.478		0.182	-0.86	-	-	43.0(0.90)	-	-	-	-
4859.039		0.32	-0.83	-	-	41.1(0.99)	-	63.6(0.80)	-	87.5(2.29)
4947.02		0.559	-1.25	109.0(2.08)	28.9(0.40)	-	-	29.5(0.85)	56.0(0.96)	62.3(2.35)
4961.387		0.631	-0.71	-	58.7(0.40)	39.0(1.18)	-	63.0(1.04)	-	-
5130.59		1.3	0.1	-	-	37.0(1.09)	-	-	-	-
5212.361		0.204	-0.87	-	123.9(0.70)	60.1(1.17)	-	87.5(1.13)	103.3(0.80)	99.6(2.41)
5255.506		0.204	-0.82	-	-	41.9(0.82)	-	83.5(0.98)	105.9(0.78)	-
5276.869		0.859	-0.44	-	-	22.4(0.82)	-	-	65.8(0.67)	-
5287.133		0.744	-1.3	101.5(2.17)	-	-	-	-	42.4(0.96)	49.5(2.31)
5293.163		0.822	-0.06	-	-	46.9(0.86)	-	-	-	-
5311.453		0.986	-0.42	-	-	-	28.2(0.71)	49.8(1.04)	58.1(0.84)	66.8(2.23)
5319.815		0.55	-0.21	-	-	63.0(0.94)	-	-	-	-
5356.967		1.264	-0.25	126.0(2.34)	-	-	-	30.90(2.51)	-	72.2(2.38)
5361.51		0.68	-0.4	-	106.9(0.65)	51.3(1.10)	-	-	94.2(0.85)	-
5371.927		1.412	0.003	-	-	-	-	-	-	-
5442.264		0.68	-0.91	143.8(2.39)	-	28.1(1.19)	-	-	71.0(0.92)	-
5718.118		1.41	-0.34	-	-	-	-	-	37.4(0.78)	-
5825.857		1.08	-0.76	-	-	-	-	-	49.4(0.93)	59.3(2.33)
4424.337	Sm II	0.485	-0.26	-	-	-	34.7(0.08)	-	-	-
4434.318		0.378	-0.576	108.3(1.14)	52.8(-0.21)	-	-	-	80.1(0.50)	-
4458.509		0.104	-1.11	-	44.3(-0.19)	-	28.0(0.05)	56.1(0.51)	67.7(0.34)	71.8(1.74)
4499.475		0.248	-1.413	81.6(1.18)	-	16.6(0.73)	-	28.3(0.42)	51.2(0.52)	59.4(1.89)
4519.63		0.543	-0.751	-	-	-	-	-	59.6(0.46)	-
4615.444		0.544	-1.262	-	-	-	-	-	25.0(0.21)	53.9(1.94)
4674.593		0.184	-1.055	-	-	-	-	-	66.3(0.28)	-
4676.902		0.04	-1.407	94.2(1.04)	-	16.3(0.46)	-	-	-	-
4704.4		0	-1.562	99.7(1.23)	-	-	-	-	-	-
4726.026		0.333	-1.849	-	-	-	-	-	22.6(0.40)	-
4791.58		0.104	-1.846	84.7(1.35)	-	-	-	25.6(0.57)	-	42.5(1.73)
4815.805		0.185	-1.501	-	23.2(-0.17)	-	-	-	45.9(0.30)	-
4844.209		0.277	-1.558	-	-	-	-	-	-	53.2(1.87)
4854.368		0.379	-1.873	44.4(1.07)	-	-	-	-	-	29.1(1.79)

The numbers in the parenthesis in columns 5 - 11 give the derived abundances from the respective line. The line information are taken from Kurucz database of atomic line lists (<https://lweb.cfa.harvard.edu/amp/ampdata/kurucz23/sekur.html>).